A Model of the Earthquake Cycle Along the San Andreas Fault System for the Past 1000 Years

Bridget R. Smith and David T. Sandwell
Institute for Geophysics and Planetary Physics
Scripps Institution of Oceanography
La Jolla, CA 92093-0225
brsmith@ucsd.edu, dsandwell@ucsd.edu

Submitted to *JGR - Solid Earth*: February 24, 2004

Abstract. We simulate 1000 years of the earthquake cycle along the San Andreas Fault System by convolving best estimates of interseismic and coseismic slip with the Green's function for a point dislocation in an elastic plate overlying a viscoelastic half-space. Interseismic slip rate is based on long-term geological estimates while fault locking depths are derived from horizontal GPS measurements. Coseismic and postseismic deformation is modeled using 70 earthquake ruptures, compiled from both historical data and paleoseismic data. This time-dependent velocity model is compared with 290 present-day geodetic velocity vectors to place bounds on elastic plate thickness and viscosity of the underlying substrate. Best-fit models (RMS residual of 2.46 mm/yr) require an elastic plate thickness greater than 60 km and a substrate viscosity between $2x10^{18}$ and $5x10^{19}$ Pa s. These results highlight the need for vertical velocity measurements developed over long time spans (> 20 years). Our numerical models are also used to investigate the 1000-year evolution of Coulomb stress. Stress is largely independent of assumed rheology, but is very sensitive to the slip history on each fault segment. As expected, present-day Coulomb stress is high along the entire southern San Andreas because there have been no major earthquakes over the past 150-300 years. Animations of the time evolution of vector displacement and Coulomb stress are available as an electronic supplement.

1. Introduction

The San Andreas Fault (SAF) System extends from the Gulf of California to the Mendocino Triple Junction and traverses many densely populated regions. This tectonically complex zone has generated at least six major earthquakes (M_w > 7.0) over past 200 years: the 1812 Wrightwood-Santa Barbara Earthquakes (M_w ~ 7.5), the 1838 San Francisco Earthquake (M_w = 7.4), the 1857 Great Fort Tejon Earthquake (M_w = 7.9), the 1868 South Hayward Earthquake (M_w = 7.0), the 1906 Great San Francisco Earthquake (M_w = 7.8), and the 1940 Imperial Valley Earthquake (M_w = 7.0). The SAF System has also produced at least 37 moderate earthquakes (M_w > 6.0) over the past 200 years. Recently, major earthquake activity has occurred primarily on faults paralleling the San Andreas Fault System, such as the 1992 Landers Earthquake (M_w = 7.3), the 1999 Hector Mine Earthquake (M_w = 7.1), and the 2003 San Simeon Earthquake (M_w = 6.8). Yet several sections of the SAF System have not ruptured during the past 150 years. These relatively long periods of quiescence, coupled with matching recurrence intervals, indicate that some segments of the San Andreas Fault System are primed for another rupture.

A major earthquake on the San Andreas Fault System has the potential for massive economic and human loss and so establishing seismic hazards is a priority [*WGCEP,* 1995; *WGNCEP*, 1999; *WGCEP*, 2003]. This involves characterizing the spatial and temporal distribution of both coseismic and interseismic deformation, as well as modeling stress concentration, transfer, and release [*Anderson et al.*, 2003]. Furthermore, it is important to understand how postseismic stress varies in both time and space and how it relates to time-dependent relaxation processes of the Earth [*Cohen*, 1999; *Kenner*, 2004]. Many questions remain regarding the characteristics of earthquake recurrence, the rupture patterns of large earthquakes [*Grant and Lettis*, 2002], and long-term fault-to-fault coupling throughout the earthquake cycle. Arrays of seismometers along the SAF System provide tight constraints on the coseismic processes of the earthquake cycle, but geodetic measurements are needed for understanding the slower processes. The large array of GPS receivers currently operating along the North American-Pacific Plate boundary has aided in the discovery of several types of aseismic slip and postseismic deformation [e.g., *Bock et al.*, 1997; *Murray and Segall,* 2001], however the 1-2 decade record is too short to sample a significant fraction of the earthquake cycle. Full 3-D, time-dependent models that span several earthquake cycles and capture the important length scales are needed to explore a range of earthquake scenarios, to provide estimates of present-day stress, and to provide insight on how

best to deploy future geodetic arrays.

Models of the earthquake cycle usually sacrifice resolution of either the space or time dimensions or are rheologically simple in order to be implemented on even the fastest modern computers. For example, time-independent elastic half-space models have been used to match geodetic observations of surface displacement of the San Andreas Fault System [e.g., *Savage and Burford,* 1973; *Li and Lim,* 1988; *Savage, 1990; Lisowski et al.,* 1991; *Feigl et al.*, 1993; *Murray and Segall,* 2001; *Becker et al.*, 2003; *Meade and Hager*, 2005]. Likewise, several local viscoelastic slip models, consisting of an elastic plate overlying a viscoelastic half-space, have been developed to match geodetically-measured postseismic surface velocities [e.g., *Savage and Prescott*, 1978; *Thatcher*, 1983; *Deng et al.*, 1998; *Pollitz et al.,* 2001; *Johnson and Segall*, 2004]. Many studies have also focused on the 3-D evolution of the local stress field due to coseismic and postseismic stress transfer [e.g., *Pollitz and Sacks,* 1992; *Stein et al.,* 1994; *Kenner and Segall*, 1999; *Freed and Lin*, 2001; *Zeng,* 2001; *Hearn et al.*, 2002; *Parsons*, 2002]. Displacement and stress models such as these have provided important constraints on fault locking depth, viscoelastic relaxation time scales, fault zone rheologies, and local fault interactions. However, because of computer speed and memory limitations, most of these numerical models are limited to a single earthquake cycle and relatively simple fault geometries.

Our objectives are to satisfy the demands of both complicated fault geometry and multiple earthquake cycles using a relatively simple layered viscoelastic model. While this is possible using purely numerical models (e.g., finite element) [e.g., *Bird and Kong*, 1994; *Furlong and Verdonck*, 1994; *Parsons*, 2002; *Segall*, 2002], studies such as these are rare due to the considerable computational requirements [*Kenner*, 2004]. Furthermore, purely numerical algorithms, implemented on even the most powerful computers, do not yet have the efficiency to explore the range of parameters that can match the geodetic observations. Therefore, improved analytic methods are essential in order to reduce the computational complexities of the numerical problem.

In a previous paper [*Smith and Sandwell*, 2004], we developed a 3-D semi-analytic solution for the vector displacement and stress tensor of an elastic plate overlying a viscoelastic half-space in response to a vertical strike-slip dislocation. The problem is solved analytically in both the vertical and time dimension (z, t), while the solution in the two horizontal dimensions (x, y) is developed in the Fourier transform domain to exploit the efficiency offered by the convolution

theorem. The restoring force of gravity is included to accurately model vertical deformation. Arbitrarily complex fault traces and slip distributions can be specified without increasing the computational burden. For example, a model computation for slip on a complex fault segment in a 2-D grid that spans spatial scales from 1 km to 2048 km requires less than a minute of CPU on a desktop computer. Models containing multiple fault segments are computed by summing the contribution for each locking depth and every earthquake for at least ten Maxwell times in the past. For example, a model for the present-day velocity, which involves 27 fault segments (each having a different locking depth) and ~100 earthquakes during a 1000-year time period, requires 230 component model computations costing 153 minutes of CPU time. Efficiency such as this enables the computation of kinematically realistic 3-D viscoelastic models spanning thousands of years.

In this paper, we apply the Fourier method to develop a kinematically realistic (i.e., secular plus episodic), time-dependent model of the San Andreas Fault System. The secular model component was largely developed in a previous publication [*Smith and Sandwell*, 2003] where we used 1099 GPS horizontal velocity measurements and long-term slip rates from geology to establish the locking depths along 18 curved fault segments. Because our initial model used a simple elastic half-space, the inferred locking depths are an upper bound; for a viscoelastic model, the apparent locking depth depends on whether velocities are measured early or late in the earthquake cycle [*Meade and Hager*, 2004]. Alternatively, the episodic model component uses a completely prescribed earthquake slip history (i.e., timing, rupture length, depth, and slip) on each fault segment for at least ten Maxwell times in the past. The timing and surface rupture for each event is inferred from published historical and paleoseismic earthquake records, as well earthquake recurrence intervals. We prescribe the rupture depth to be equal to the present-day locking depth and prescribe the amount of slip on each rupture to be equal to the slip rate times the time since the previous earthquake on that segment. Note that these simplifying assumptions do not allow for partial slip or spatially overlapping ruptures. The complete model (secular plus episodic components) is matched to the present-day vector GPS data to solve for elastic plate thickness, half-space viscosity, geologic Poisson's ratio (i.e., representing the compressibility of the elastic plate at infinite timescales), and apparent locking depth factor. Finally, the best-fit model is used to estimate secular and postseismic Coulomb stress change within the seismogenic layer. While this kinematic model of the entire San Andreas Fault System is one of the first of

its kind to consider deformation changes over the past millennium, this is a difficult problem and future studies using more realistic rheologies and earthquake slip histories will certainly help further bound the solution. Nevertheless, this work provides new insights into the physics of the earthquake cycle and will hopefully improve future seismic hazard analyses of the San Andreas Fault System.

2. Great Earthquakes of the SAF System: 1000 A.D. to Present Day

While present-day motion of the San Andreas Fault System is continuously monitored by contemporary geodetic techniques, deformation occurring prior to the modern era is highly uncertain [*Toppozada et al.*, 2002]. However, historians and paleoseismologists have worked to piece together evidence for past seismic activity on the San Andreas Fault System over the past 1000 years and beyond. These efforts make up two earthquake databases: 1) historical earthquakes, based on written records and personal accounts [e.g., *Bakun*, 1999; *Toppozada et al.,* 2002], and 2) prehistorical earthquakes, or events estimated from paleoseismic trench excavations [e.g., *Sieh et al.*, 1989; *Fumal et al.*, 1993]. The prehistorical earthquake record of the San Andreas Fault System is based on a collaborative effort from many workers of the paleoseismic community [*Grant and Lettis*, 2002 and references therein] and provides estimates for past earthquake ages dating back to 500 A.D. in some locations. A variety of dating methods have been used for these estimates, including radiocarbon dating, tree ring dating, earthquake-induced subsidence, and sea level changes. Alternatively, the historical earthquake records spans the past ~200 years and is bounded by the establishment of Spanish missions along coastal California in the early 1770s. Missionary documents existed sporadically from about 1780 to 1834, at which point all missions were secularized. Soon following the 1849 California Gold Rush, newspapers were regularly published, providing the San Francisco Bay region with the most complete earthquake record of this time. Based on the increase in California population and published newspapers in the following years, it is likely that the historical earthquake record is complete for $M > 6.5$ events from about 1880 and for $M > 6.0$ events from about 1910 [*Toppozada et al.*, 1981; *Agnew*, 1991]. For the period of modern instrumentation, the earthquake record for $M = 5.5$ events is complete in southern California starting in 1932 [*Hileman et al.*, 1973] and beginning in 1942 in northern California [*Bolt and Miller*, 1975].

2.1 Historical Earthquakes

From evidence gathered to date [*Jennings*, 1994; *Bakun*, 1999; *Toppozada et al*., 2002], the San Andreas Fault System has experienced a rich seismic history over the past ~ 200 years, producing many significant earthquakes (Figure 1, Table 1). From 1812 to 1906, four major earthquakes (M > 7.0) were recorded on two main sections of the fault system. In the southern-central region of the system, a pair of major earthquakes occurred when the 1812 rupture was overlapped by the major event of 1857. Likewise, another pair of major earthquakes were recorded on the northern region of the fault system, where faulting of the Great 1906 event overlapped the rupture of the 1838 earthquake. In addition, significant events of M ~ 7 occurred in 1868 and 1989 in the San Francisco Bay area on the Hayward fault and in the Santa Cruz Mountains near Loma Prieta, respectively, and in 1940 near the Mexican border on the Imperial fault.

While over 35 significant earthquakes (M≥ 6.0) have ruptured the San Andreas Fault System and caused significant damage over the past 200 years (Table 1), quiescent periods following events greater than M = 7.0 indicate that only earthquakes of this size relieve significant tectonic stress [*Toppozada et al*, 2002]. We will further address this hypothesis later in the text, but for now it is worthwhile to briefly review these major events that ruptured the San Andreas Fault System:

December 1812 – Wrightwood-Santa Barbara

The first major historical earthquake known to rupture the San Andreas Fault System took place on December 8, 1812, near the town of Wrightwood [*Toppozada et al*., 2002], causing damage in regions such as San Juan Capistrano, San Gabriel, and San Fernando. This event was previously thought to have occurred near San Juan Capistrano [*Toppozada et al*., 1981], although *Jacoby et al*. [1988] more recently determined that it was likely associated with a San Andreas rupture that damaged major branches and root systems of trees near Wrightwood in 1812, as inferred from tree ring data. Thirteen days later, on December 21, 1812, a second major earthquake was reported and strongly felt in the Santa Barbara region (often referred to as the Santa Barbara Earthquake) [*Toppozada et al*., 1981]. Although neither the epicenters nor rupture extents of these two events were clearly defined, it is likely that both were centered on two approximate halves of a total rupture that extended ~170 km from Cajon Pass to Tejon Pass

[*Toppozada et al.*, 2002; *Jacoby et al.*, 1988]. *Deng and Sykes* [1996] calculated the change in Coulomb stress for a northwest trending rupture on the Mojave segment of the San Andreas fault terminating near Pallet Creek and showed that a rupture on December 8th of this segment would have promoted a second rupture further to the northwest, suggested to be the December 21st event. The combination of the two 1812 events caused damage in both Orange and Santa Barbara Counties; extreme shaking forced the toppling of a church tower at the San Juan Capistrano Mission, killing 40 people [*Toppozada et al.*, 2002].

June 1838 – San Francisco-San Juan Bautista

Following the establishment in 1776 of the Mission San Francisco Dolores in San Francisco, the first major event on the northern San Andreas Fault System was observed in 1838. Extensive damage from this earthquake, unsurpassed by any other historical earthquake other than the Great 1906 quake, was noted throughout the Bay Area from San Francisco in the north to Monterey in the south [*Toppozada et al.*, 2002]. Personal accounts describe large ground cracks and broken redwood trees [*Bakun, 1999*; *Louderback*, 1947]. Faulting extent has been suggested from San Francisco to San Juan Bautista due to aftershock activity and reports of extensive damage.

January 1857 – The Great Fort Tejon Earthquake

The Great Fort Tejon Earthquake (M = 7.9) was the largest event ever recorded in California and one of the greatest events on record in the United States. It ruptured the southern San Andreas fault from San Bernardino County in the south to Monterey County in the north [*Wood*, 1955; *Sieh*, 1978a] and left a ~350 km long surface scar in its wake. Two foreshocks, occurring approximately 1-2 hours before the main shock, were identified by *Sieh* [1978b] just north of Parkfied. It is likely that faulting began in this region, traversed southeastward, and terminated at Cajon Pass [*Toppozada et al.*, 2002]. The southern portion of this event faulted the same portion of the San Andreas as did the 1812 earthquake sequence thirty years prior. Strong shaking caused by the 1857 earthquake lasted for at least one minute, causing severe damage as far as Ventura [*Townley,* 1939*; Agnew and Sieh,* 1978]. Fortunately, the 1857 main shock was to blame for only one death due to the lack of major structures near the ruptured fault. A few structures in downtown Los Angeles, 60 km from the fault, were reportedly cracked, while much

stronger damage was sited in San Fernando, approximately 40 km from the rupture [*Agnew and Sieh*, 1978].

October 1868 – The Hayward Earthquake

The 1868 event on the south Hayward fault, a branch of the northern San Andreas Fault System, was the largest earthquake to hit the Bay Area since the 1838 San Andreas event, although seismic activity was very high during the ~10 years leading up to this event. The Hayward rupture extended ~ 50 km southward from the Oakland region [*Yu and Segall*, 1996] and caused 30 deaths [*Toppozada et al*., 2002]. Although rupture did not actually occur on the San Andreas, much of San Francisco was damaged by this major Bay Area earthquake. Following the 1868 Hayward Earthquake, seismicity levels dropped significantly and remained low for approximately 13 years [*Toppozada et al*., 2002].

April 1906 – The Great San Francisco Earthquake

The Great 1906 San Francisco Earthquake (M = 7.8), the largest historical earthquake of northern California, ruptured the northern San Andreas fault for over 430 km from San Juan Bautista in the south to Shelter Cove in the north. The 1906 San Andreas event re-ruptured portions of the 1838 rupture from San Juan Bautista to San Francisco. Extensive damage resulted from northern Monterey County to southern Humboldt County. Even inland regions like Napa were significantly damaged. Shaking was estimated at over one minute; the quake was felt from southern Oregon to south of Los Angeles and inland as far as central Nevada [*Ellsworth*, 1990]. Over 3000 deaths and more than 225,000 injures were attributed to the quake and the fire storm that followed due to downed power lines.

May 1940 – The Imperial Valley Earthquake

Known as the strongest recorded historical earthquake to hit the Imperial Valley of southern California, the 1940 earthquake ruptured over 30 km of the Imperial fault and also extended ~60 km southeast of Brawley [*Stein and Hanks*, 1998]. Severe property damage devastated the El Centro region where nine people lost their lives. Irrigation systems were extensively damaged and railroad tracks were bent out of line where they crossed the Imperial fault in three separate locations [*Ulrich,* 1941]. At least 5.8 m of right-lateral displacement were observed on the

Imperial fault [*Toppozada et al.*, 2002]. This significant M7.0 southern California earthquake was felt as far away as Los Angeles and Tucson, Arizona.

The remaining historical earthquakes of the San Andreas Fault System over the past 200 years include at least thirteen earthquakes in southern California (1875, 1890, 1892, 1899, 1906, 1918, 1923, 1948, 1954, 1968, 1979, 1986, and 1987), over nine earthquakes in northern California (1858, 1864, 1890, 1897, 1898, 1911, 1984, and 1989), and the repeated sequence along the Parkfield segment in central California (1881, 1901, 1922, 1934, 1966, and 2004) [*Toppozada et al.*, 2002; *Jennings*, 1994; *Langbein*, 2004; *Murray et al.*, 2004]. Alternatively, the creeping zone of the San Andreas, bounded by the Parkfield segment to the south and the San Andreas-Calaveras split to the north, is noticeably void of large historical earthquakes; this is because tectonic plate motion is accommodated by creep instead of a locked fault at depth. While other portions of the SAF System have been known to accommodate plate motion through creeping mechanisms [e.g., *Burgmann et al.*, 2000; *Lyons and Sandwell*, 2003], we assume that the remaining sections of the fault zone are locked at depth throughout the interseismic period of the earthquake cycle to ensure a coseismic response at known event dates. It is also important to note that while we have cautiously adopted realistic rupture scenarios based on information available in the literature, some poorly constrained events, particularly those without a mapped surface rupture, have been approximately located. We have chosen pre-defined fault segments that simplify the model organization without entirely compromising the locations and hypothesized rupture extents of historical earthquakes.

2.2 Prehistorical Earthquakes

In addition to the recorded earthquake data available, rupture history of the San Andreas Fault System from paleoseismic dating can be used to estimate prehistorical events (Table 2). Paleoseismic trenching at nineteen sites (Figure 1) has allowed for estimates of slip history along the primary trace of the San Andreas, along the Imperial fault, along the northern San Jacinto fault, and at one site on the Hayward fault. These data contribute greatly toward understanding the temporal and spatial rupture history of the San Andreas Fault System over multiple rupture cycles, particularly during the past few thousand years where seismic events can only be assumed based on recurrence interval estimates. For example, while the recurrence interval of

the Imperial fault segment is estimated to be ~ 40 years [*WGCEP*, 1995], *Thomas and Rockwell* [1996] found that no major earthquakes prior to the 1940 and 1979 events have produced significant surface slip over the past 300 years. *Fumal et al*. [2002b] document the occurrence of at least four surface-rupturing earthquakes along the southern San Andreas strand near the Thousand Palms site during the past 1200 years. Likewise, excavations at Burro Flats, Plunge Creek, and Pitman Canyon along the southern San Andreas strand [*Yule*, 2000; *McGill et al*., 2002] provide age constraints for at least five prehistoric events during the past 1000 years. Along the San Jacinto strand, *Rockwell et al*. [2003] estimate at least five paleoevents at Hog Lake over the past 1000 years. *Fumal et al*. [2002a], *Biasi et al*. [2002], and *Lindevall et al*. [2002] report evidence for 5-6 surface-rupturing events in total at the Wrightwood, Pallet Creek, and Frazier Mountain trench sites along the Big Bend of the San Andreas. Further to the north, trenching at Bidart Fan [*Grant and Sieh*, 1994] reveal three prehistoric events, while at Las Yeguas, *Young et al*. [2002] estimate at least one event between Cholame Valley and the Carrizo Plain. In northern California, *Knudsen et al*. [2002] interpret several episodes of sea level change (earthquake-induced subsidence) along the northern section of the San Andreas at Bolinas Lagoon and Bodego Harbor and compare evidence for two 1906-like ruptures from work done by *Cotton et al*. [1982], *Schwartz et al*. [1998], *Heingartner* [1995], *Prentice* [1989], *Niemi and Hall* [1992], *Niemi* [1992], *Noller* [1993], *Baldwin* [1996], and *Simpson et al*. [1996]. And lastly, excavations of the southern Hayward fault at Tyson's Lagoon [*Lienkaemper et al*., 2002] reveal evidence for at least three paleoseismic events over the past millennium. While uncertainty ranges for paleoseismic dating can be fairly large, we do our best to adhere to the results of experts in the field and estimate prehistorical earthquake dates, locations, and rupture extents based on their findings. These earthquakes, in addition to the known historical ruptures discussed above, will be used in the subsequent 3-D viscoelastic model of San Andreas Fault System deformation of the past 1000 years.

3. 3-D Viscoelastic Model

For purposes of investigating the viscoelastic response over multiple earthquake cycles, we apply a semi-analytic Fourier model (Appendix) to the geometrically complex fault setting of the San Andreas Fault System. The model consists of an elastic plate (of thickness H) overlying a viscoelastic half-space. Faults within the elastic plate extend from the surface to a prescribed

locking depth (d). Below the locked faults, fully-relaxed secular slip (assuming infinite time) takes place down to the base of the elastic plate. The model is kinematic, given that the time, extent, and amount of slip is prescribed. Coseismic slip occurs on prescribed fault segments and the amount of slip is based on slip deficit assumptions. Transient deformation follows each earthquake due to viscoelastic flow in the underlying half-space. The duration of the viscoelastic response, characterized by the Maxwell time, depends on the viscosity of the underlying half-space and the elastic plate thickness.

The complete earthquake cycle is modeled with two components: secular and episodic. The secular model simulates interseismic slip that occurs between the fault locking depth and the base of the elastic plate (d to H, Figure A1). We construct this secular model in two parts (geologic + shallow backslip). First, we permit fully-relaxed slip over the entire thickness of the elastic plate (0 to H) – the geologic, or block, model. Second, secular backslip within the locked fault region (0 to d) compensates for shallow slip deficit – the backslip model. The episodic model (or earthquake-generating model) prescribes slip over the locked section of each fault segment (0 to d). Fault slip rate, historical/pre-historical earthquake sequence, and recurrence intervals are used to establish the magnitude of coseismic slip events. Slip amounts are determined by multiplying the slip rate of each ruptured fault segment by either the time spanning the previous event, if one exists, or the recurrence interval time if no previous event exists.

The numerical aspects of this approach involve generating a grid of vector force couples that simulate complex fault geometry, taking the 2-D horizontal Fourier transform of the grid, multiplying by the appropriate transfer functions and time-dependent relaxation coefficients, and finally inverse Fourier transforming to obtain the desired results [*Smith and Sandwell*, 2004]. The solution satisfies the zero-traction surface boundary condition and maintains stress and displacement continuity across the base of the plate (Appendix). A far-field velocity step across the plate boundary of 40 mm/yr is simulated using a cosine transform in the x-direction (i.e., across the plate boundary). The far-field boundary condition at the top and bottom of the grid is simulated by arranging the fault trace to be cyclic in the y-direction (i.e., parallel to the plate boundary). In this analysis, we solve for four variable model parameters: elastic plate thickness (H), half-space viscosity (η), geologic Poisson's ratio (ν_g), and locking depth factor (f_d). We assume fixed values for the shear modulus μ = 28 GPA, Young's modulus E = 70 GPA,

Poisson's ratio (episodic model) $\nu = 0.25$, density $\rho = 3300\ \mathrm{kg/m^3}$, and gravitational acceleration $g = 9.81\ \mathrm{m/s^2}$. The entire computational process for a single time-step requires ~ 40s for a grid size of 2048 x 2048 elements, the size used for this analysis. This complete fault model will be used to efficiently explore the 3-D viscoelastic response of the upper mantle throughout the 1000-year San Andreas Fault System earthquake cycle.

4. Application to the San Andreas Fault System

We apply the 3-D viscoelastic model described above to study deformation and stress associated with fault segments of the San Andreas Fault System. We refine a fault segmentation scheme of a previous elastic half-space analysis [*Smith and Sandwell*, 2003], obtained from digitizing the major fault strands along the SAF System from the *Jennings* [1994] fault map; segmentation modifications were made in order to better accommodate along-strike variations in fault-segmented ruptures. We group the San Andreas Fault System into 27 main fault segments, comprised of over 400 elements, spatially consistent with previous geologic and geodetic studies. The fault system is rotated about its pole of deformation (52°N, 287°W) [*Wdowinski et al.*, 2001] into a new co-ordinate system, after which fault segments are embedded in a grid of 2048 elements along the SAF System (*y*-direction) and 1024 elements across the system (*x*-direction) with a grid spacing of 1 km. The large grid width of 1024 km is needed to accurately model the flexural wavelength of the elastic plate. The fault model includes the following primary segments (Figure 2, Table 3): Imperial, Brawley, Coachella-San Andreas, Palm Springs-San Andreas, San Bernardino Mountains-San Andreas, Superstition, Borrego-San Jacinto, Coyote Creek-San Jacinto, Anza-San Jacinto, San Jacinto Valley, San Jacinto Mountains, Mojave, Carrizo, Cholame, Parkfield Transition, San Andreas Creeping, Santa Cruz Mountains-San Andreas, San Francisco Peninsula-San Andreas, North Coast-San Andreas, South-Central Calaveras, North Calaveras, Concord, Green Valley-Bartlett Springs, South Hayward, North Hayward, Rodgers Creek, and Maacama.

We assume that slip rate, locking depth, and recurrence interval remain constant along each fault segment (Table 3) and that the system is loaded by stresses extending far from the locked portion of the fault. Each fault segment is assigned a deep slip rate based on geodetic measurements, geologic offsets, and plate reconstructions [*WGCEP,* 1995, 1999]. In some cases, slip rates were adjusted (+/- 5 mm/yr on average) in order to satisfy an assumed far-field plate

velocity of 40 mm/yr. We adopt locking depths from a previous inversion of the Southern California Earthquake Center (SCEC) Crustal Motion Map (version 3; *Shen et al*. [2003]) using a complimentary elastic half-space model [*Smith and Sandwell*, 2003]. Because these depths are based on purely elastic assumptions, we allow the entire set of locking depths to be adjusted in our parameter search through a locking depth factor (f_d). Due to the large uncertainty in locking depth for the Superstition segment reported by *Smith and Sandwell* [2003], we arbitrarily set this locking depth to 7 km. Likewise, we adjusted the locking depth of the South-Central Calaveras segment to 7 km to allow for episodic coseismic events. Recurrence intervals for each segment were adopted from various sources [*WGCEP*, 1995, 1999; *WGNCEP*, 1996] and estimate the time span between characteristic earthquakes on each fault segment where no prehistorical data are presently available.

In addition to the above faulting parameters, we also define the temporal sequence and rupture length of past earthquakes ($M \geq 6.0$) based on the earthquake data history discussed in Section 4.2. We estimate calendar year rupture dates and surface ruptures on fault segments as identified by Table 3. For years 1812-2004, fault segments rupture coseismically according to their historical earthquake sequence. For years prior to 1812, we estimate prehistorical ruptures by calculating the average date from the paleoseismological evidence summarized in Table 2 and extrapolating rupture lengths to our defined fault segments based on discussions provided by the relevant references. It should also be noted that we include the recent coseismic/postseismic response of both the 1992 $M_w = 7.3$ Landers Earthquake and the 1999 $M_w = 7.1$ Hector Mine Earthquake (Figure 1, Table 1), both occurring west of the SAF System in the Eastern California Shear Zone (ECSZ). These two earthquakes have been studied in detail [e.g., *Savage and Svarc*, 1997; *USGS et al.,* 2000*; Sandwell et al.,* 2002*; Fialko et al.,* 2001; *Fialko*, 2004b] and well-constrained surface slip models and seismic moment estimates are available. To simplify the model, we specify slip on both Landers and Hector Mine fault planes by assuming that slip is constant with depth and solving for a slip depth that preserves seismic moment. For the Landers Earthquake, we use a seismic moment of 1.1×10^{20} Nm [*Fialk*o, 2004b] and adopt a fault locking depth of 16 km. For the Hector Mine Earthquake, we use a seismic moment of 5×10^{19} Nm [*Fialko et al*., 2001] and adopt a fault locking depth of 12 km.

5. Geodetic Data

Continuously operating GPS networks offer a way to track ground motions over extended periods of time [*Bock et al.,* 1997; *Nikolaidis*, 2002], and because of the large collection of data, also offer both horizontal *and* vertical estimates of crustal deformation. While horizontal GPS velocity estimates over the past three decades have commonly been used to constrain fault models, estimates of vertical velocity typically accompanied large observational uncertainties and were disregarded. However, these measurements may play an important role in establishing the rheological structure of the Earth's crust and underlying mantle [*Deng et al.*, 1998; *Pollitz et al.*, 2001]. Consequently, we use both horizontal and vertical velocity estimates from the Scripps Orbit and Permanent Array Center (SOPAC) from 315 stations within our region of study, operating for ~10 years. The SOPAC Refined Velocity data set contains estimated velocities through 2004 using a model that takes into account linear velocity, co-seismic offsets, postseismic exponential decay, and annual/semi-annual fluctuations [*Nikolaidis*, 2002]. To increase data coverage in northern California and in the Parkfield region, we added five data subsets (containing a total of 120 stations) from the US Geologic Survey (USGS) (both automatic and network (Quasi-Observational Combined Analysis [*Dong et al.*, 1998]) processing schemes). While data from eight campaigns were initially explored, only five of these (FtIrwin, MedicineLake, NorthSanFranciscoBay, SFBayArea, and Parkfield) were utilized in the final analysis due to reasons discussed below. While not entirely continuous (some data were gathered campaign-mode), most of the USGS data were collected from stations in operation for ~ 4 - 7 years.

The data were first refined by excluding all stations with velocity uncertainties (either horizontal or vertical) greater than 3 mm/yr. All remaining stations were subjected to an initial round of modeling, where outliers were removed that were both anomalous compared to their neighbors and had velocity model misfits greater than 10 mm/yr. Furthermore, preliminary least squares analyses revealed that velocities with small uncertainty estimates (< 0.5 mm/yr) dominated most of the weighted RMS model misfit and thus were adjusted to comply with a prescribed lower bound of 0.5 mm/yr. The remaining 292 stations with velocities satisfying these constraints form our total GPS velocity data set (Figure 2) and combine to form a total of 876 horizontal and vertical velocity measurements spanning much of the San Andreas Fault System. While the spatial distribution is not as complete as the SCEC Crustal Motion Map

[*Shen et al.*, 2003] distribution, preliminary tests showed that vertical velocity information, not currently available from SCEC, provide an important constraint of the viscoelastic properties of the model.

6. Results

A least squares parameter search was used to identify optimal parameters for elastic plate thickness (H), half-space viscosity (η), geologic Poisson's ratio (ν_g), and locking depth factor (f_d). Plate thickness affects the amplitude and wavelength of deformation and also plays a role in the timescale of observed deformation, particularly in the vertical dimension [*Smith and Sandwell*, 2004]. Thick elastic plate models yield larger-wavelength postseismic features but shorten the duration of the vertical response compared to thin plate models. Half-space viscosity determines how quickly the model responds to a redistribution of stress from coseismic slip. High viscosities correspond to a large response time while low viscosities give rise to more rapid deformation. Variations in Poisson's ratio ($\nu = 0.25$ - 0.45) determine the compressibility of the elastic material over varying timescales. Over geologic time, tectonic strains are large and thus elastic plates may behave like an incompressible fluid ($\nu \sim 0.5$). Alternatively, over short timescales, strains are smaller and plates may behave more like an elastic solid ($\nu = 0.25$). We adjust Poisson's ratio of the geologic model component only (ν_g, observed at infinite time), requiring the episodic model to behave as an elastic solid. Lastly, we allow the entire set of locking depths to vary simultaneously using a single factor f_d to scale the purely elastic estimates from *Smith and Sandwell* [2003]. This scaling depends largely upon the thickness of the elastic plate [*Thatcher*, 1983].

6.1 Present-day Velocity

Our best model is found by exploring the parameter space and minimizing the weighted residual misfit, χ^2, of the geodetic data set and the present day (calendar year 2004) modeled velocity field. The data misfit is defined by

$$V_{res}^{i} = \frac{V_{gps}^{i} - V_{m}^{i}}{\sigma^{i}} \quad \text{and} \quad \chi^2 = \frac{1}{N}\sum_{i=1}^{N}\left(V_{res}^{i}\right)^2,$$

where V_{gps} is the geodetic velocity estimate, V_m is the model estimate, σ^i is the uncertainty of the i^{th} geodetic velocity, and N is the number of geodetic observations. The parameter search is executed in two phases and involves sixteen free parameters. First, two unknown horizontal velocity components for each of the six GPS networks (SOPAC + five USGS data sets) are estimated by removing the mean misfit from a starting model. This exercise linearly shifts all horizontal data into a common reference frame. Second, we fix the ten velocity components and perform a 4-dimensional parameter search for elastic plate thickness, half-space viscosity, geologic Poisson's ratio, locking depth factor.

Before modeling, we calculate an unweighted RMS of 7.8439 mm/yr and a weighted RMS of 14.37 (dimensionless) for the 876 GPS velocity components. We begin with a starting model that has H = 50 km, η = 1x10^{19} Pa s, ν_g = 0.25, and f_d = 1. After adjusting the ten unknown velocity components for the starting model, a 4-dimensional parameter search is performed to locate the best-fitting model. Using over 140 trial models, the best model is identified, resulting in a weighted RMS residual of 4.5034 (2.4599 mm/yr unweighted), thus reducing the total variance of the data by over 90%. Individually, the x, y, and z velocity misfits vary considerably, producing weighted and unweighted RMS residuals of 4.29 (2.19 mm/yr), 5.20 (2.72 mm/yr), and 3.95 (2.45 mm/yr), respectively.

Optimal parameters for this model are H = 70 km, η = 3x10^{18} Pa s, ν_g = 0.40, and f_d = 0.70, although a large span of parameters fit the model nearly as well (Figure 3). From these results, we place both upper and lower bounds on model parameters for a range of acceptable models. The weighted RMS residual is minimized for a plate thickness of 70 km, although the misfit curve significantly flattens for ~ H > 60 km. Lower and upper bounds for half-space viscosity are 1x10^{18} and 5x10^{19} Pa s. The best-fitting geologic Poisson's ratio is 0.40, although models with f_d = 0.35 – 0.45 also fit well. And finally, the best-fit locking depth factor is 0.70, although models with f_d = 0.65 – 0.80 are also acceptable.

Comparisons between the model fault-parallel velocity and the GPS data for eight fault corridors are shown in Figure 4. Each model profile is acquired along a single fault-perpendicular trace, while the geodetic measurements are binned within the fault corridors and projected onto the perpendicular trace, thus some of the scatter is due to projection of the data onto a common profile. While the model accounts for most of the observed geodetic deformation, there are some local systematic residuals that require deformation not included in

our model. For example, GPS velocities in the Eastern California Shear Zone are underestimated (Figure 4, Profiles 2-5), as we do not incorporate faults in the Owens Valley, Panamint Valley, and Death Valley fault zones. [e.g., *Bennett et al.*, 1997; *Hearn et al.*, 1998, *Dixon et al.*, 2000; *Gan et. al.,* 2000; *McClusky et al.*, 2001; *Miller et al.*, 2001; *Peltzer et al.*, 2001; *Dixon et al.*, 2003]. Observed differences in the model are also due to approximations in the earthquake record, including the timing of prehistorical earthquakes, the rupture extent of both pre- and historical earthquakes, and our assumption of complete seismic moment release.

Results for the fault-perpendicular velocity model are shown in Figure 5a. The fault-perpendicular model has a pronounced west-trending (negative) zone of deformation (~ -2.5 mm/yr) to the west of the Mojave and Carrizo segments, while a complimentary diffuse east-trending (positive) region (~ 1.5 mm/yr) is observed to the northeast. An interesting butterfly-like feature is also noted along the creeping segment, just north of Parkfield. This feature is due the abrupt change in locking depth from the north (0 km) to the south (10.2 km). An unusual zone of deformation to the north of Parkfield has also been noted by other workers [*S. Wdowinski*, personal communication].

In addition, vertical deformation (Figure 5b) is in general agreement with geodetic measurements and reveals similar features to our previous elastic half-space model [*Smith and Sandwell*, 2003]. Uplift in the regions of the San Bernardino Mountains and Mojave segments is due to the associated compressional bends [*Williams and Richardson*, 1991], while subsidence is observed in extensional regimes such as the Brawley segment (Salton Trough). The large lobate regions, such as the pair noted to the east and west of the Parkfield segment, are attributed to the combined effects of the creeping section and the long-standing strain accumulation along the 1857 Fort Tejon rupture. A future event similar to the 1857 rupture would significantly reduce the magnitude of these lobate features.

A time series of models spanning several earthquake cycles (Movie 1) shows that the vertical deformation pattern accumulates displacement during the interseismic period that is fully relaxed during the postseismic phase, such that long-term vertical deformation from repeated earthquake cycles is zero. Both horizontal velocity components maintain secular deformation features throughout the earthquake cycle, except of course when an earthquake is prescribed and an appropriate coseismic response is observed. Large horizontal transients, lasting ~ 5-20 years,

depending on the event, are only observed after the largest of earthquakes (e.g., 1812, 1857, 1868, 1906, 1940).

6.2 Present-day Coulomb Stress

Deep, secular slip along the San Andreas Fault System induces stress accumulation in the upper locked portions of the fault network. Because our model has complete slip release during each earthquake, the stress essentially drops to zero with the exception of postseismic transients. We use our semi-analytic model and the parameters described in Section 6.1 to calculate stress due to interseismic, coseismic, and postseismic phases of the earthquake cycle. The model (Appendix) provides the three-dimensional vector displacement field from which we compute the stress tensor. The stress tensor is computed along each fault segment and is resolved into shear stress, τ, and normal stress, σ_n, on the nearby fault segment to form the Coulomb failure function, σ_f

$$\sigma_f = \tau - \mu_f \sigma_n,$$

where μ_f is the effective coefficient of friction [*King et al.,*1994; *Simpson and Reasenberg*, 1994]. Right-lateral shear stress and extension are positive and we assume μ_f = 0.6. The calculations do not include the stress accumulation due to compression or extension beneath the locked portions of each fault segment. Because Coulomb stress is zero at the surface and becomes singular at the locking depth, we calculate the representative Coulomb stress at 1/2 of the local locking depth [*King et al.*, 1994]. This calculation is performed on a fault-segment by fault-segment basis for the San Andreas Fault System from earthquakes over the past 1000 years (Figure 6).

The present-day (calendar year 2004) model predicts quasi-static Coulomb stress along most fault segments ranging from 1-7 MPa (Figure 6c). Typical stress drops during major earthquakes are ~ 5 MPa and so the model provides compatible results to seismological constraints. Regions of reduced stress include the Parkfield, Superstition, Borrego, Santa Cruz Mountains, and South Calaveras segments where there has either been a recent (within the last 20 years) earthquake or Coulomb stress accumulation rate is low due to fault geometry and locking depth [*Smith and Sandwell*, 2003]. Alternatively, high stress regions include most of the southern San Andreas

from the Cholame segment to the Coachella segment, the northern-central portion of the San Jacinto fault, and along the eastern Bay Area, where major earthquakes are possible. It should also be noted, although not evident in the present-day model capture (except in the Parkfield vicinity), that the model demonstrates a small, negative stress behavior due to time-dependent postseismic readjustment, commonly referred to as the stress shadow [*Harris*, 1998; *Kenner and Segall*, 1999]. Animations of stress evolution (Movie 2) for years 1800-2004 show the spatial decay and magnitude of stress shadows following earthquake events, particularly evident in major events such as the 1857 Fort Tejon and 1906 San Francisco earthquakes [*Harris and Simpson*, 1993, 1996, 1998; *Kenner and Segall*, 1999; *Parsons*, 2002]. These animations show how locked fault segments eventually become re-loaded with tectonic stress as relaxation ceases, resulting in positive stress accumulation surrounding the fault and a resumption of the earthquake cycle.

7. Discussion

7.1 Implications of Best-Fit Model Parameters

The best-fitting model of our least-squares analysis results in relatively thick elastic plate (70 km) and a moderate half-space viscosity ($3x10^{18}$ Pa s). Because the model represents both the lower crust and upper mantle as a single element, the half-space viscosity that we solve for reflects an average of the two values. A viscosity of $3x10^{18}$ Pa s, corresponding to a relaxation time of ~ 7 years, is likely a lower bound. However, a wide range of acceptable parameters have been reported by other studies. *Li and Rice* [1987] report viscosity values of $2x10^{19}$ to $1x10^{20}$ Pa s from geodetic strain data on the San Andreas fault, assuming a lithospheric thickness of about 20-30 km. Alternatively, *Pollitz et al.* [2001] assume an upper layer viscosity of $4x10^{17}$ Pa s to model deformation due to the 1999 Hector Mine earthquake in the Mojave desert. More recently, *Johnson and Segall* [2004] estimated an elastic thickness of 44 -100 km and a viscosity of $1x10^{19}$ – $2.9x10^{20}$ Pa s for central California using Southern California Earthquake Center (SCEC) GPS velocities and triangulation measurements of postseismic strain following the 1906 San Francisco Earthquake. In comparison, investigations of post-glacial rebound infer whole-mantle viscosities on the order of 10^{22} Pa s. Rebound estimates such as these tend to be uniformly higher than those determined from seismic studies, perhaps because the larger-scale rebound pattern samples far deeper into the mantle than the more localized fault deformation

pattern. It may also be true that seismically-determined viscosities include a larger transient effect, although these hypotheses are nearly impossible to test without additional, long-term geodetic observations.

While our estimate of plate thickness may seem larger than those typically cited in the literature, such differences may be related to different timescales of crustal loading. The elastic plate thickness is defined as the elastically strong portion of the crust and mantle that is responsible for supporting topographic loads; this region typically achieves isostatic equilibrium in 1-10 Ma [*Nishimura and Thatcher*, 2003]. Geophysical observations that sample this 'geologically-long' time period may result in a different (lower) estimate of elastic plate thickness than observations of stress relaxation over much shorter times. For example, models based on gravity-topography relations [*Lowry et al.*, 2000], effectively accounting for 1 Myr of loading, yield elastic plate thickness values of ~5-15 km in the western U.S. Likewise, *Iwasaki and Matsu'ura* [1982] report estimates of elastic thickness of 23-40 km based on isostatic rebound (~ 2000 years) from the draining of pluvial lakes. In addition, *Nishimura and Thatcher* [2003] use 30 years of leveling data of the Basin and Range to arrive at an elastic plate thickness of 38 +/- 8 km. In this study, we use continuously operating GPS data capturing stress loading due to postseismic recovery limited to the past ~10 years. Thus our lower bound estimate of ~60 km may be an artifact of the relatively-short observation period of the data used. This value is in agreement with the 40-100 km estimate of *Johnson and Segall* [2004], however, we stress the need for additional far-field data to place better constraints on this parameter.

A model of finite plate thickness, as opposed to one representing an infinite elastic medium, broadens the observed model velocity step and requires a reduced locking depth to match the GPS data. We find that locking depths for a 70 km thick elastic plate are about 30% less than those needed for an elastic half-space model [*Smith and Sandwell*, 2003]. An important aspect of the plate model is that far-field deformation is partitioned into separate secular and post-seismic parts according to the ratio of the elastic plate thickness and the fault segment locking depth [*Savage and Prescott*, 1978; *Ward*, 1985; *Smith and Sandwell*, 2004]. Immediately following an earthquake, the step in velocity across the fault will match the full geological velocity prescribed on the fault in accordance with an elastic half-space model. After several Maxwell times, the step will broaden and be reduced in amplitude. For example, the Mojave region has a locking depth of ~20 km, which is roughly 30% of the elastic plate thickness.

Therefore, only 70% of the far-field deformation is accommodated by the secular model. The remaining 30% of the far-field deformation results from repeated earthquakes. Elastic half-space block models do not contain this important physics and therefore estimated locking depths will be systematically too large and estimated slip rates will be systematically too low [*Meade and Hager*, 2005].

The model uses two Poisson's ratios depending on the timescale of the deformation process. The cyclical earthquake process (interseismic backslip and coseismic forward slip) is modeled using a standard Poisson's ratio for an elastic solid ($\nu = 0.25$). However, for geologic timescales ($t = \infty$; secular geologic model component), we allow the model to accommodate changes in Poisson's ratio (ν_g), assuming that plates accumulate large tectonic strains over geologic timescales, which in turn alter the compressibility of the material. We began the modeling process using a Poisson's ratio of 0.25 for both timescales but found that the vertical deformation associated with the geologic portion of the model displayed unreasonable features in zones of known compression and extension. When Poisson's ratio was increased to ~0.45 for the geologic model, the vertical deformation became sensible for compressional and extensional features, regardless of elastic plate thickness. Since this parameter has an important effect on the vertical component of the model, we included it as a free parameter. Our parameter search identified an optimal Poisson's ratio of $\nu_g = 0.40$ for the geologic model, producing realistic secular vertical features and indicating a preference for a more incompressible elastic plate over geologic timescales.

7.2 Temporal and Spatial Deficiencies of GPS Data

While we have identified a set of model parameters that minimize the residual data misfit, the available geodetic data do not distinctly prefer one set of model parameters over a variety of alternative ones. It is possible that additional data, particularly in areas of sparse coverage, would provide tighter bounds on rheological parameters. Data in northern California, for example, in comparison to those available in southern California, are sparse and thus provide weaker constraints on the model parameters for the northern California region. This is unfortunate, as many earthquakes have occurred along the northern portion of the SAF System and may contribute significantly to the overall deformation field. Furthermore, far-field data are lacking for the entire plate boundary. While the near-field horizontal GPS data provide tight

constraints on slip rate and locking depth, the far-field vertical GPS data constrain the elastic plate thickness. The important length scale is the flexural wavelength and for a 70-km thick plate, the wavelength is about 400-500 km, thus vertical GPS measurements acquired ~200 km from the fault zone provide critical information.

In an attempt to understand how results differ for horizontal and vertical geodetic velocity observations, preliminary analyses using the SCEC Crustal Motion Map 3.0 [*Shen et al.*, 2003] (horizontal velocity estimates only) were first performed, although parameter results trended toward an elastic plate thickness of 100 km and greater with no global minimum. These results imply a preference for a model of infinite elastic thickness, demonstrating that an elastic half-space model can be used to accurately model horizontal geodetic data only [*Smith and Sandwell*, 2003; *Becker et al.*, 2004; *Mead and Hager*, 2005]. Thus vertical velocity estimates are necessary for constraining viscoelastic model parameters [*Deng et al.*, 1998; *Pollitz et al.*, 2001]. Vertical data from the next release of the SCEC velocity model, combined with future estimates from the Plate Boundary Observatory, will provide better constraints in future models.

7.3 Present-day Stress Implications and Seismic Hazard

The actual stress along the San Andreas Fault System consists of the cyclical stress due to the earthquake cycle that we have estimated with our model, plus some background time-invariant stress field that is not modeled. Likewise, for this hazard assessment we have not considered dynamic stress changes due to nearby coseismic events. These can be significantly larger than the static stress and may play an important role in modeling of the stress field, particularly for non-bilateral ruptures [*Kilb*, 2002]. Nevertheless, assume for a moment that the present day Coulomb stress model (Figure 6c) is an acceptable portrait of accumulated tectonic stress on the SAF System. Based on this idea, we can calculate how this model compares to historical stress distributions, earthquake epicenters, and known surface ruptures. Figure 6(a,b) shows snapshots of the stress field prior to the 1812 Wrightwood and the 1857 Fort Tejon earthquakes, demonstrating the state of stress prior to the two most significant historical earthquakes along the southern San Andreas. According to our model, moderate stress levels had been reached along the Mojave segment prior to the 1812 event (Figure 6a). While the epicenter(s) of the 1812 events are poorly known, it is reasonable to assume that peak stress levels of 5-10 MPa on the segment were enough to generate a large earthquake. Alternatively, the stress field prior to the

1857 Fort Tejon event indicates a significantly high amount of stress in the vicinity of the estimated epicenter (Figure 6b). Based on the behavior of these events, it is conceivable that the Mojave section of the SAF is presently experiencing a stress level (~5-7 MPa) similar to the stress level before the 1812 event. In contrast, the Carrizo and Cholame sections are presently experiencing lower stress levels than those indicated by our model prior to the 1857 event. Comparing this information with the present-day model, it is likely that most of the southern San Andreas and portions of the San Jacinto may be on the verge of a major earthquake, particularly along the San Bernardino Mountains and Coachella sections where the last known event dates back to 1690 [*WGCEP*, 1995]. Again, this discussion implicitly assumes that the likelihood and size of an earthquake depends only on the static stress accumulated since the last earthquake.

Justifying the extent of surface rupture for historical earthquakes and relating this to the present-day model requires further examination. While the events of 1812 relieved significant stress on the Mojave segment, the 1857 event 30 years later also ruptured this segment in addition to those to the north. According to our model, stress levels prior to the 1857 event were very high for the Cholame and Carrizo segments of the SAF, but were significantly lower for the Mojave portion. The Mojave segment does not indicate exceedingly high accumulation rates and in fact shows lower than average rates due to its faulting geometry and deep locking depth [*Smith and Sandwell*, 2003]. So why did the 1857 rupture propagate through this segment? Two explanations are plausible: 1) the 1812 event did not actually rupture this entire segment of the SAF, or 2) the 1812 event, and possibly many others, did not release its entire amount of accumulated interseismic moment and portions of this segment where indeed primed for another rupture only 30 years later. We prefer to eliminate the first explanation, as recent studies [*Jacoby et al.*, 1988; *Deng and Sykes*, 1996; *Toppozada et al.*, 2002] show excellent correlation for rupture on the Mojave segment in 1812. The suggestion of incomplete interseismic moment release appears more likely, with evidence for such behavior demonstrated by the 2004 M6.0 Parkfield Earthquake [e.g., *Langbein et al.*, 2004; *Lienkaemper et al.*, 2004; *Murray et al.*, 2004]. Assuming that the Parkfield segment, which last ruptured in 1966, accumulated slip at a rate of 40 mm/yr over 40 years, this segment had accumulated at least 1.5 m of slip. Yet preliminary results indicate that the 2004 Parkfield event generated only 33 cm of coseismic slip [*Murray et al.*, 2004]. If our model is designed to generate coseismic slip according to purely kinematic assumptions, resulting in, for example, 1.5 m of slip at Parkfield in 2004, then we have obviously

overestimated slip and stress drop in some occurrences. Future adjustments to this approach will need to be investigated by implementing actual historical seismic moments.

8. Conclusions

In summary, we have employed a previously-developed 3-D semi-analytic viscoelastic model [*Smith and Sandwell*, 2004] to estimate the velocity and stress accumulation along the entire San Andreas Fault System. Geometric complications of the fault system have no effect on the speed of the computation as 2-D convolutions are performed in the Fourier transform domain. Moreover, since the solution is analytic in time, no numerical time-stepping is needed. A model consisting of hundreds of fault elements embedded in a 2048 x 2048 grid requires less than 40s of CPU time on a desktop computer. A new model is computed for each locking depth, each earthquake, and each epoch, where, for example, a 1000-year simulation involving over 230 individual model computations can be computed in ~ 3 hours. This efficiency enables the computation of kinematically realistic 3-D viscoelastic models spanning thousands of years.

We use this method to estimate interseismic, coseismic, and postseismic deformation of the San Andreas Fault System over the past 1000 years. Both horizontal and vertical components of GPS-derived velocities (over 800 combined rates and uncertainties) that capture present-day plate motion are used to solve for elastic plate thickness (H), half-space viscosity (η), geologic Poisson's ratio (ν_g), and locking depth factor (f_d). A least-squares parameter search over more than 100 models results in model parameters of H = 70 km, $\eta = 3\text{x}10^{18}$ Pa s, $\nu_g = 0.40$, and f_d = 0.70 with a 4.091 weighted RMS misfit and a 90% data variance reduction. From analysis of Coulomb stress near the major fault strands, we find regions of elevated interseismic stress along most of the southern San Andreas and the northern San Jacinto, reflecting the 150^+ years that have transpired since a major seismic rupture occurred on specific fault segments.

While we believe that the differences between the model and the geodetic velocity data are primarily due to an imprecise knowledge of past earthquakes, there are also limitations to our model. Rheology of the crust and upper mantle is more complex than our single-layer laterally homogeneous model, both in the horizontal [*Malservisi et al.*, 2001] and in the vertical direction [*Pollitz et al.*, 2001]. We have ignored several important processes such as changes in local pore-pressure [*Massonnet et al.*, 1996; *Peltzer et al.*, 1996; *Fialko*, 2004a], laterally varying rheology, and non-linear postseismic response [*Freed and Burgmann*, 2004]. Horizontal misfits

are higher in the ECSZ than elsewhere, suggesting unmodeled strain accumulation. Nevertheless, this simple viscoelastic model provides an improved representation of crust-mantle rheology when compared to the elastic half-space model and the agreement with existing geodetic data is encouraging.

While this study is the first of its kind to jointly consider geodetic and paleoseismic data in a large-scale, long-term model of the San Andreas Fault System, we admit that the entire deformation problem is a difficult one to solve and that future studies using more realistic rheologies and earthquake slip histories will certainly help further bound the solution. Yet perhaps the most important result of this study is a quantitative evaluation of elevated seismic hazards along specific areas of the San Andreas Fault System where a future major earthquake is more likely to occur. While models such as these are not yet capable of predicting the timing and extent of future ruptures, they are an important tool for understanding how different sections of the San Andreas Fault System store energy and release stress over time and the implications of these processes for future deformation.

9. Acknowledgements

We thank Yehuda Bock and Rosanne Nikolaidis for providing the SOPAC Refined Velocity data set. We also thank the U.S. Geological Survey for providing supplemental GPS velocity measurements. We thank Bruce Bills, Debi Kilb, Yuri Fialko, Catherine Johnson, and Duncan Agnew for providing careful in-house reviews of draft versions of the manuscript. We also thank Tony Watts for the useful discussions he provided pertaining to crustal loading timescales and Frank Vernon for his advice regarding the use of paleoseismic data. This research was supported by the NASA Earth System Science Fellowship Program (ESSF-0131) and the NSF Earth Science Program (EAR-0105896).

10. Appendix 3-D Viscoelastic Body Force Model

The Fourier model [*Smith and Sandwell*, 2004] consists of a grid of body-force couples (representing multiple fault elements) embedded in an elastic plate overlying a viscoelastic half-space (Figure A1). The solutions that make up this model are based on the previous work of *Steketee* [1958], *Rybicki* [1971], *Nur and Mavko* [1974], and *Rundle and Jackson* [1977], who developed the first pieces of a 3-D analytic viscoelastic solution (i.e., Green's function) based on

dislocation solutions. While the Green's function is computationally efficient for calculating displacement or stress at a few points due to slip on a small number of faults, it is less efficient for computing deformation on large grids representing fault systems, especially when the fault system has hundreds or thousands of segments. Because the force-balance equations are linear, the convolution theorem can be used to speed the computation. This substantially reduces the computational burden associated with an arbitrarily complex distribution of force couples necessary for fault modeling.

We begin by solving for the displacement vector $\mathbf{u}(x,y,z)$ due to a point vector body force at depth. The following text provides a brief outline of our mathematical approach while a more detailed derivation can be found in *Smith and Sandwell* [2004]. The full derivation and source code are available at http://topex.ucsd.edu/body_force.

(1) Develop differential equations relating a three-dimensional (3-D) vector body force to a 3-D vector displacement. To partially satisfy the boundary condition of zero shear traction at the surface, an image source [*Weertman*, 1964] is applied at a mirror location in the vertical direction.

(2) Take the 3-D Fourier transform to reduce the partial differential equations to a set of linear algebraic equations.

(3) Invert the linear system of equations to obtain the 3-D displacement vector solution.

(4) Perform the inverse Fourier transform in the z-direction (depth) by repeated application of the Cauchy Residue Theorem.

(5) Introduce a layer of thickness H into the system through an infinite summation of image sources [*Weertman*, 1964; *Rybicki*, 1971], reflected both above and below the surface $z = 0$.

(6) Integrate the point source Green's function over depths $[d_1, d_2]$ to simulate a vertical fault plane. For the general case of a dipping fault, this integration can be done numerically.

(7) Analytically solve for Maxwell viscoelastic time-dependence using the Correspondence Principle and assuming a Maxwell time defined by $\tau_m = 2\eta/\mu$. Following an approach similar to that of *Savage and Prescott* [1978], we map time and viscosity into an implied half-space shear modulus. We require the bulk modulus to remain constant and thus also solve for an implied Young's modulus.

(8) Calculate the non-zero normal traction at the surface and cancel this traction by applying an equal but opposite vertical load on an elastic layer over a viscoelastic half-space, similar to the Boussinesq Problem.

While this approach is an efficient way to address elaborate faulting and complex earthquake scenarios, it also incorporates a new analytic solution to the vertical loading problem for an elastic plate overlying a viscoelastic half- space where the gravitational restoring force is included. The development of this analytic solution follows the approach of *Burmister* [1943] and *Steketee* [1958], but uses computer algebra to analytically invert a 6 by 6 matrix of boundary conditions.

The numerical aspects of this approach involve generating grids of vector force couples (i.e., F_x, F_y, and F_z) that simulate complex fault geometry, taking the Fourier transform of the grid, multiplying by the Fourier transform of the Green's function of the model, and finally, taking the inverse Fourier transform of the product to obtain the displacement or stress field. Arbitrarily complex curved and discontinuous faults can easily be converted to a grid of force vectors. The model parameters are: plate thickness (H), locking depths (d_1, d_2), shear modulus (μ), Young's modulus (E), density (ρ), gravitational acceleration (g), half-space viscosity (η), and Poisson's ratio (ν). The solution satisfies the zero-traction surface boundary condition and maintains stress and displacement continuity across the base of the plate [see *Smith and Sandwell*, 2004]. The x-boundary condition of constant far-field velocity difference across the plate boundary is simulated using a cosine transform in the x-direction. The y-boundary condition of uniform velocity in the far-field is simulated by arranging the fault trace to be cyclic in the y-dimension.

Using this approach, the horizontal complexity of the model fault system has no effect on the speed of the computation. For example, computing vector displacement and stress on a 2048 x 2048 grid for a fault system consisting of 400 segments and a single locking depth requires less than 40 seconds of CPU time on a desktop computer. Because multiple time steps are required to fully capture viscoelastic behavior, a very efficient algorithm is needed for computing 3-D viscoelastic models with realistic 1000-year recurrence interval earthquake scenarios in a reasonable amount of computer time (i.e., days).

11. References

Agnew, D.C. (1991), How complete is the pre-instrumental record of earthquake in Southern California, in *Environmental Perils: San Diego Region*, P. L. Abbott and W. J. Elliott (editors), San Diego Association of Geologists, San Diego.

Agnew, D.C., and K.E. Sieh (1978), A documentary study of the felt effects of the great California earthquake of 1857, *Bull. Seismol. Soc. Am.*, 68, 1717-1729.

Anderson, G., B. Aagaard, and K. Hudnut (2003), Fault interactions and large complex earthquakes in the Los Angeles area, *Science*, 302, 1946-1949.

Bakun, W. (1999), Seismic Activity of the San Francisco Bay Region, *Bull. Seismol. Soc. Am.*, 89, 764-784.

Bakun, W.H., and C.M. Wentworth (1997), Estimating earthquake location and magnitude from seismic intensity data, *Bull. Seismol. Soc. Am.*, 87, 1502-1521.

Baldwin, J.N. (1996), Paleoseismic investigation of the San Andreas fault on the north coast segment, near Machester, California, *M.S. Thesis*, San Jose State University, California, 127 pp.

Becker, T.W., J. Hardebeck, and G. Anderson (2004), Constraints on fault slip rates of the southern California plate boundary from GPS velocity and stress inversions, *Geophys. J. Int.*, doi:10.1111/j.1365-246X.2004.02528.x.

Bennett, R.A., B.P. Wernicke, J.L. Davis, P. Elosegui, J.K. Snow, M.J. Abolins, M.A. House, G.L. Stirewalt, and D.A. Ferrill (1997), Global Positioning System constraints on fault slip rates in the Death Valley region, California and Nevada, *Geophys. Res. Lett.*, 24, 3073-3076.

Biasi, G.P., R.J. Weldon II, T.E. Fumal, and G.G. Seitz (2002), Paleoseismic event dating and the conditional probability of large earthquake on the southern San Andreas fault, California, *Bull. Seismol. Soc. Am.*, 92, 2761-2781.

Bird, P., and X. Kong (1994), Computer simulations of California tectonics confirm very low strength of major faults, *Geo. Soc. Am. Bull.*, 106, 159-174.

Bock Y., S. Wdowinski, P. Fang, J. Zhang, J. Behr, J. Genrich, S. Williams, D. Agnew, F. Wyatt, H. Johnson, K. Stark, B. Oral, K. Hudnut, S. Dinardo, W. Young, D. Jackson, and W. Gurtner (1997), Southern California Permanent GPS Geodetic Array: Continuous measurements of crustal deformation between the 1992 Landers and 1994 Northridge earthquakes, *J. Geophys. Res.*, 102, 18,013-18,033.

Bolt, B.A., and R.D. Miller (1975), Catalogue of earthquakes in northern California and adjoining areas, 1 January 1910-31 December 1972, Seismographic Stations, University of California, Berkeley, California, 567 pp.

Burgmann, R., D. Schmidt, R.M. Nadeau, M. d'Alessio, E. Fielding, D. Manaker, T.V. McEvilly, and M.H. Murray (2000), Earthquake potential along the northern Hayward fault, California, *Science*, 289, 1178-1182.

Burmister, D.M. (1943), The theory of stresses and displacements in layered systems and applications of the design of airport runways, paper presented at the Annual Meeting, Highway Res. Board, Natl. Res. Counc., Washington, D.C.

Cohen, S.C. (1999), Numerical Models of Crustal Deformation in Seismic Zones, *Adv. Geophys*, 41, 133-231.

Cotton, W.R., N.T. Hall, and E.A. Hay (1982), Holocene behavior of the San Andreas fault at Dogtown, Point Reyes National Seashore, California, *U.S. Geol. Survey Open File Rept*. 80-1142, 33pp.

Deng, J., and L.R. Sykes (1996), Triggering of 1812 Santa Barbara earthquake by a great San Andreas shock: implications of future seismic hazards in southern California, *Geophys. Res. Lett.,* 23, 1155-1158.

Deng, J., M. Gurnis, H. Kanamori, and E. Hauksson (1998), Viscoelastic flow in the lower crust after the 1992 Landers, California, earthquake, *Science*, 282, 1689-1692.

Dixon, T.H., M. Miller, F. Farina, H. Wang, and D. Johnson (2000), Present-day motion of the Sierra Nevada block and some tectonic implications for the Basin and Range Province, North American Cordillera, *Tectonics*, 19, 1-24.

Dixon, T.H., E. Norabuena, and L. Hotaling (2003), Paleoseismology and Global Positioning System; earthquake-cycle effects and geodetic versus geologic fault slip rates in the Eastern California Shear Zone, *Geology*, 31, 55-58.

Dong, D., T.A. Herring, and R.W. King (1998), Estimating Regional Deformation from a Combination of Space and Terrestrial Geodetic Data, *J. Geodesy*, 72, 200-214.

Ellsworth, W.L. (1990), Earthquake history, 1769-1989, chap. 6 of Wallace, R.E., ed., The San Andreas Fault System, California: *U.S. Geo. Surv. Prof. Pap*. 1515, 152-187.

Fialko, Y. (2004a), Evidence of fluid-filled upper crust from observations of post-seismic deformation due to the 1992 M_w 7.3 Landers earthquake, *J. Geophys. Res.*, 109, doi:10.1029/2003JB002985.

Fialko, Y. (2004b), Probing the mechanical properties of seismically active crust with space geodesy: Study of the co-seismic deformation due to the 1992 M_w 7.3 Landers (southern California) earthquake, *J. Geophys. Res.*, 109, doi:10.1029/2003JB002756.

Fialko, Y., M. Simons, and D. Agnew (2001), The complete (3-D) surface displacement field in the epicentral area of the 1999 M_w7.1 Hector Mine earthquake, California, from space geodetic observations, *Geophys. Res. Lett.*, 28, 3063-3066.

Feigl, K.L., D.C. Agnew, Y. Bock, D. Dong, A. Donnellan, B.H. Hager, T.A. Herring, D.D. Jackson, T.H. Jordan, R.W. King, S. Larsen, K.M. Larson, M.H. Murray, Z. Shen, and F.H. Webb (1993), Space geodetic measurements of crustal deformation in Central and Southern California, 1984-1992*, J. Geophys. Res.*, 98, 21, 677-21,712.

Freed, A.M., and R. Burgmann (2004), Evidence of power-law flow in the Mojave desert mantle, *Nature*, 430, 548-551.

Freed, A.M., and J. Lin (2001), Delayed triggering of the 1999 Hector Mine earthquake by viscoelastic stress transfer, *Nature*, 411, 180-183.

Fumal, T.E., S.K. Pezzopane, R.J. Weldon II, and D.P. Shwartz (1993), A 100-year average recurrence interval for the San Andreas fault at Wrightwood, California, *Science*, 259, 199-203.

Fumal, T.E., R.J. Weldon II, G.P. Biasi, T.E. Dawson, G.G. Seitz, W.T. Frost, and D.P. Schwartz (2002a), Evidence for large earthquakes on the San Andreas fault at the Wrightwood, California, paleoseismic site: A. D. 500 to Present, *Bull. Seismol. Soc. Am.*, 92, 2726-2760.

Fumal, T.E., M.J. Rymer, and G.G. Seitz (2002b), Timing of large earthquake since A. D. 800 on the Mission Creek strand of the San Andreas Fault Zone at Thousand Palms Oasis, near Palm Springs, California, *Bull. Seismol. Soc. Am.*, 92, 2841-2860.

Furlong, K.P., and D. Verdonck (1994), Three-dimensional lithospheric kinematics in the Loma Prieta region, California: Implications for the earthquake cycle, in *The Loma Prieta, California, earthquake October 17, 1989 – Tectonic processes and models*, edited by R. W. Simpson, *U.S. Geol. Surv. Prof. Pap.*, 1550-F, F103-F131.

Gan, W., J.L. Svarc, J.C. Savage, and W.H. Prescott (2000), Strain accumulation across the Eastern Caliornia Shear Zone at latitude 36 degrees 30 N, *J. Geophys. Res.*, 105, 16,229-16,236.

Grant, L.B., and W.R. Lettis (2002), Introduction to the Special Issue on Paleoseismology of the San Andreas Fault System, *Bull. Seismol. Soc. Am.*, 92, 2552-2554.

Grant, L.B., and K. Sieh (1994), Paleoseismic evidence of clusered earthquakes on the San Andreas fault in the Carrizo Plain, California, *J. Geophys. Res.*, 99, 6819-6841.

Harris, R.A. (1998), Introduction to special section: Stress triggers, stress shadows, and implications for seismic hazard, *J. Geophys. Res.*, 103, 24,347-24,358.

Harris, R.A., and R.W. Simpson (1993), In the shadow of 1857: An evaluation of the static stress changes generated by the M8 Ft. Tejon, California, earthquake, *Eos Trans. AGU*, 74, Fall Meet. Suppl., 427.

Harris, R.A., and R.W. Simpson (1996), In the shadow of 1857 – The effect of the great F. Tejon earthquake on subsequent earthquakes in southern California, *Geophys. Res. Lett.*, 23, 229-232.

Harris, R.A., and R.W. Simpson (1998), Suppression of large earthquakes by stress shadows: A comparison of Coulomb and rate-and-state failure, *J. Geophys. Res.*, 103, 24,439-24,452.

Hearn, E.H., and E.D. Humphreys (1998), Kinematics of the southern Walker Lane Belt and motion of the Sierra Nevada block, California, *J. Geophys. Res.*, 103, 27,033-27,049.

Hearn, E.H., R. Bürgmann, R., and R.E. Reilinger, Dynamics of Izmit Earthquake Postseismic Deformation and Loading of the Düzce Earthquake Hypocenter, *Bull. Seismol. Soc. Am.*, 92, 172-193, 2002.

Heingartner, G.F. (1995), Paleoseismic recurrence investigation of the Santa Cruz Mountains segment of the San Andreas fault near Watsonville, California, *M.S. Thesis*, San Jose State University, California, 136 pp.

Hileman, J.A., C.R. Allen, and J.M. Nordquist (1973), *Seismicity of the Southern California Region, 1 January 1932 to 21 December 1972*, California Institute of Technology, Pasadena, Seismological Laboratory Contribution 2385, 81 pp.

Iwaski, T., and M. Matsu'ura (1982), Quasi-static crustal deformations due to a surface load, *J. Phys. Earth*, 30, 469-508.

Jacoby, G., P. Sheppard, and K. Sieh (1988), Irregular recurrence of large earthquakes along the San Andreas fault: evidence from trees, *Science*, 241, 196-199.

Jennings, C.W. (1994), Fault activity map of California and adjacent areas with locations and ages of recent volcanic eruptions: California Division of Mines and Geology Data Map Series No. 6, 92, 2 plates, map scale 1:750,000.

Johnson, K.M., and P. Segall (2004), Viscoelastic earthquake cycle models with deep stress-driven creep along the San Andreas fault system, *J. Geophys. Res.*, 109, doi:10.1029/2004JB003096.

Kenner, S.J. (2004), Rheological controls on fault loading rates in northern California following the 1906 San Francisco earthquake, *Geophys. Res. Lett.*, 31, doi: 10.1029/2003GL018903.

Kenner, S., and P. Segall (1999), Time-dependence of the stress shadowing effect and its relation to the structure of the lower crust, *Geology*, 27, 119-122.

Kilb, D. (2003), A strong correlation between induced peak dynamic Coulomb stress change from the 1992 M7.3 Landers earthquake and the hypocenter of the 1999 M7.1 Hector Mine earthquake, *J. Geophys. Res.,* 108, doi:10.1029/2001JB000678.

King. G.C.P., R.S. Stein, and J. Lin (1994), Static stress changes and the triggering of earthquakes, *Bull. Seismol. Soc. Am.*, 84, 935-953.

Knudsen, K.L., R.C. Witter, C.E. Garrison-Laney, J.N. Baldwin, and G.A. Carver (2002), Past earthquake-induced rapid subsidence along the northern San Andreas fault: a paleoseismological method for investigating strike-slip faults, *Bull. Seismol. Soc. Am.*, 92, 2612-2636.

Langbein, J.H., A. Snyder, Y. Bock, and M.H. Murray (2004), Deformation from the 2004 Parkfield, California, Earthquake measured by GPS and creepmeters, *EOS Trans. AGU 85(47)*, Fall Meet. Suppl., Abstract S51C-0170F.

Langbein, J.H. (2004), Overview of the 2004 M6 Parkfield, California, Earthquake, *EOS Trans. AGU 85(47)*, Fall Meet. Suppl., Abstract S53D-02.

Li., V.C., and H.S. Lim (1988), Modeling surface deformations at complex strike-slip plate boundaries, *J. Geophys. Res.*, 93, 7943-7954.

Li, V.C., and J.R. Rice (1987), Crustal deformation in great California earthquake cycles, *J. Geophys. Res.*, 92, 11,530-11,551.

Lienkaemper, J.J., T.E. Dawson, S.F. Personius, G.G. Seitz, L.M. Reidy, and D.P. Schwartz (2002), A Record of Large Earthquakes on the southern Hayward fault for the past 500 years, *Bull. Seismol. Soc. Am.*, 92, 2637-2658.

Lienkaemper, J.J., B. Baker, and F.S. McFarland (2004), Slip in the 2004 Parkfield, California, Earthquake Measured on Alinement Arrays, *EOS Trans. AGU 85(47)*, Fall Meet. Suppl., Abstract S54B-01.

Lindvall, S.C., T.K. Rockwell, T.E. Dawson, J.G. Helms, K.W. Bowman (2002), Evidence for two surface ruptures in the past 500 years on the San Andreas fault at Frazier Mountain, California, *Bull. Seismol. Soc. Am.*, 92, 2689-2703.

Lisowski, M., J.C. Savage, and W.H. Prescott (1991), The velocity field along the San Andreas fault in central and southern California, *J. Geophys. Res.*, 96, 8369-8389.

Louderback, G.D. (1947), Centeral California earthquakes of the 1830's, *Bull. Seismol. Soc. Am.* 37, 33-74.

Lowry, A.R., N.M. Ribe, and R. B. Smith (2000), Dynamic elevation of the Cordillera, western United States, *J. Geophys. Res.*, 105, 23,371-23,390.

Lyons, S., and D. Sandwell (2003), Fault creep along the southern San Andreas from interferometric synthetic aperature radar, permanent scatterers, and stacking,, *J. Geophys. Res.*, 108, 10:1029/2002JB001831.

Malservisi, R., K.P. Furlong, and T.H. Dixon (2001), Influence of the earthquake cycle and lithospheric rheology on the dynamics of the eastern California shear zone, *Geophys. Res. Lett.*, 28, 2731-2734.

Massonnet, D., W. Thatcher, and H. Vadon (1996), Radar interferometry detects two mechanism of postseismic relaxation following the Landers, California earthquake, *Nature*, 382, 612-612.

McClusky, S., S.C. Bjornstad, B.H. Hager, R.W. King, B.J. Meade, M.M. Miller, F.C. Monastero, and B.J. Souter (2001), Present day kinematics of the Eastern California Shear Zone from a geodetically constrained block model, *Geophys. Res. Lett.*, 28, 3369-3372.

McGill, S., S. Dergham, D. Barton, T. Berney-Ficklin, D. Grant, C. Hartling, K. Hobart, R. Minnich, M. Rodriguez, E. Runnerstrom, J. Russell, K. Schmoker, M. Stumfall, J. Townsend, and J. Williams (2002), Paleoseismology of the San Andreas fault at Plunge Creek, near San Bernardino, southern California, *Bull. Seismol. Soc. Am.*, 92, 2803-2840.

Meade, B.J., and B.H. Hager (2004), Viscoelastic deformation for a clustered earthquake cycle, *Geophys. Res. Lett.*, 31, doi:10.1029/2004GL019643.

Meade, B.J., and B.H. Hager (2005), Block Models of Crustal Motion in Southern California Constrained by GPS Measurements, *J. Geophys. Res*, in press.

Miller, M.M., D.J. Johnson, T.H. Dixon, and R.K. Dokka (2001), Refined kinematics of the Eastern California Shear Zone from GPS observations, 1992-1998, *J. Geophys. Res.,* 106, 2245-2263.

Murray, M.H., and P. Segall (2001), Modeling broadscale deformation in northern California and Nevada from plate motions and elastic strain accumulation, *Geophys. Res. Lett.*, 28, 3215-4318.

Murray, J.R., P. Segall, and J. Svarc (2004), Slip in the 2004 Parkfield M6 Earthquake: Comparison With Previous Events and Implications for Earthquake Recurrence Models, *EOS Trans. AGU 85(47)*, Fall Meet. Suppl., Abstract S54B-03.

Nikolaidis, R. (2002), Observation of Geodetic and Seismic Deformation with the Global Positioning System, *Ph.D. Thesis*, Univ. of Calif. San Diego, 2002.

Niemi, T.M. (1992), Late Holocene slip rate, prehistoric earthquakes, and Quaternary neotectonics of the northern San Andreas fault, Marin County, California, *Ph.D. Thesis*, Stanford University, Palo Alto, California, 199 pp.

Niemi, T.M., and N.T. Hall (1992), Late Holocene slip rate and recurrence of great earthquakes on the San Andreas fault in northern California, *Geology*, 20, 195-198.

Nishimura, T., and W. Thatcher (2003), Rheology of the lithosphere inferred from postseismic uplift following the 1959 Hebgen Lake earthquake, *J. Geophys. Res.*, 108, doi:10.1029/2002JB002191.

Noller, J.S., K.I. Kelson, W.R. Lettis, K.A. Wickens, G.D. Simpson, K. Lightfoot, T. Wake (1993), Prelimilary characterizations of Holocene activity on the San Andreas fault based on offset archaeologic sites, F. Ross State Historic Park, California, *U.S. Geol. Surv. NEHRP Final Tech. Rep.*

Nur, A., and G. Mavko (1974), Postseismic viscoelastic rebound, *Science*, 183, 204-206.

Parsons, T. (2002), Post-1906 stress recovery of the San Andreas fault system calculated from three-dimensional finite element analysis, *J. Geophys. Res.*, 107, doi:10.1029/2001JB001051.

Peltzer, G., F. Crampe, S. Hensley, and P. Rosen (2001), Trasient strain accumulation and fault interaction in the Eastern California Shear Zone, *Geology*, 29, 975-978.

Peltzer, G.P., P. Rosen, F. Rogez, and K. Hudnut (1996), Postseismic rebound in fault step-overs caused by pore fluid flow, *Science*, 273, 1202-1204.

Pollitz, F.F., C. Wicks, and W. Thatcher (2001), Mantle flow beneath a continental strike-slip fault: Postseismic deformation after the 1999 Hector Mine earthquake, *Science*, 293, 1814-1818.

Pollitz F., and S. Sacks (1992), Modeling of postseismic relaxation following the great 1857 earthquake, Southern California, *Bull. Seismol. Soc. Am.*, 82, 454-480.

Prentice, C.S. (1989), Earthquake geology of the northern San Andreas fault near Point Arena, California, *Ph.D. Dissertation*, California Institute of Technology, Pasadena, California, 252 pp.

Rockwell, T.K., J. Young, G. Seitz, A. Meltzner, D. Verdugo, F. Khatib, D. Ragona, O. Altangerel, and O. Altangerel (2003), 3,000 years of ground-rupturing earthquakes in the Anza Seismic Gap, San Jacinto Fault, Southern California: Time to shake it up?, 2003 SCEC Annual Meeting, *Proceedings and Abstracts*, 13.

Rundle, J.B., and D.D. Jackson (1977), A three-dimensional viscoelastic model of a strike slip fault, *Geophys. J. Roy. Astron. Soc.*, 49, 575-591.

Rybicki, K. (1971), The elastic residual field of a very long strike-slip fault in the presence of a discontinuity, *Bull. Seismol. Soc. Am.* 61, 72-92.

Sandwell, D.T., Sichiox, L., and B. Smith (2002), The 1999 Hector Mine Earthquake, Southern California: Vector Near-Field Displacements from ERS InSAR, *Bull. Seismol. Soc. Am.*, 92, 1341-1354.

Savage, J.C. (1990), Equivalent strike-slip earthquake cycles in half-space and lithosphere-asthenosphere earth models, *J. Geophys. Res., 95*, 4873-4879.

Savage, J.C., and W.H. Prescott (1978), Asthenosphere readjustment and the earthquake cycle, *J. Geophys. Res.*, 83, 3369-3376.

Savage, J.C., and R.O. Burford (1973), Geodetic determination of relative plate motion in central California, *J. Geophys. Res., 78*, 832-845.

Savage, J.C., and J.L. Svarc (1997), Postseismic deformation associated with the 1992 M_w = 7.3 Landers earthquake, southern California, *J. Geophys., Res.*, 102, 7565-7577.

Schwartz, D.P., D. Pantosti, K. Okumura, T.J. Powers, and J.C. Hamilton (1998), Paleoseismic investigations in the Santa Cruz Mountains California: implications for recurrence of large-magnitude earthquakes on the San Andreas fault, *J. Geophys. Res.* 103, 17,985-18,001.

Segall, P. (2002), Integrating geological and geodetic estimates of slip rate on the San Andreas fault system, *Int. Geol. Rev.*, 44, 82.

Sharp, R.V. (1980), 1940 and Prehistoric earthquake displacement on the Imperial fault, Imperial and Mexicali Valleys, California and Mexico, in *California Seismic Safety Commission Symposium Proceedings, The Human Settlements on the San Andreas Fault*, pp. 68-81, Calif. Seismic Safety Comm., Sacramento.

Shen, Z.K., D.C. Agnew, and R.W. King (2003), The SCEC Crustal Motion Map, Version 3.0, http://epicenter.usc.edu/cmm3.

Sieh, K.E. (1978a), Slip along the San Andreas fault associated with the great 1857 earthquake, *Bull. Seismol. Soc. Am.*, 68, 1421-1448.

Sieh, K.E. (1978b), Central California foreshocks of the great 1857 earthquake, *Bull. Seismol. Soc. Am.*, 68, 1731-1749.

Sieh, K.E., M. Stuiver, and D. Brillinger (1989), A more recise chronology of earthquake produced by the San Andreas fault in Southern California, *J. Geophys. Res.*, 95, 603-623..

Simpson, R.W., and P.A. Reasenberg (1994), Earthquake-induced static stress changes on central California faults, *U.S. Geo. Surv. Prof. Paper 1550-F*, F55-F89.

Simpson, G.D., J.S. Noller, K.I. Kelson, and W.R. Lettis (1996), Logs of trenches across the San Andreas fault, Archae camp, Fort Ross State Historic Park, Northern California, U.*S. Geol. Surv. NEHRP Final Tech. Rept.*

Smith, B.R., and D.T. Sandwell (2003), Coulomb Stress along the San Andreas Fault System*, J. Geophys. Res.*, 108, doi:10.1029/2002JB002136.

Smith, B.R., and D.T. Sandwell (2004), A 3-D Semi-Analytic Viscoelastic Model for Time-Dependent Analyses of the Earthquake Cycle, *J. Geophys. Res.*, 109, doi:10.1029/2004JB003185.

Stein, R.S. (1987), Contemporary plate motion and crustal deformation, *Rev. Geophys.,* 25, 855-863.

Stein, R.S., G.C.P. King, and J. Lin (1994), Stress triggering of the 1994 M = 6.7 Northridge, California, earthquake by its predecessors*, Science*, 265, 1432-1435.

Stein, R.S., and T.C. Hanks (1998), M > 6 earthquakes in southern California during the twentieth century: no evidence for a seismicity or moment deficit, *Bull. Seismol. Soc. Am.*, 99, 635-652.

Steketee, J.A. (1958), On Volterra's dislocations in a semi-infinite elastic medium, *Can. J. Phys.*, 36, 192-205.

Thatcher, W. (1983), Nonlinear strain buildup and the earthquake cycle on the San Andreas Fault, *J. Geophys. Res.*, 88, 5893-5902.

Thomas, A.P., and T.K. Rockwell (1996), A 300- to 550- year history of slip on the Imperial fault near the U.S.–Mexico border: Missing slip at the Imperial fault bottleneck, *J. Geophys. Res.*, 101, 5987-5997.

Toppozada, T.R., D.M. Branum, B.S. Reichle, and C.L. Hallstrom (2002), San Andreas Fault Zone, California: M >5.5 Earthquake History, *Bull. Seismol. Soc. Am.*, 92, 2555-2601.

Toppozada, T.R., C.R. Real, and D.L. Parke (1981), Preparation of isoseismal maps and summaries of reported effects for pre-1900 California earthquakes, *Calif. Div. Mines Geol. Open File Rept. 81-11SAC*, 182 pp.

Toppozada T.R., and D. Branum (2002), California M> 5.5 earthquakes, history and areas damaged, in *International Handbook of Earthquake and Engineering Seismology*, W.H. Lee, H. Kanamori, and P. Jennings (Editors), International Association of Seismology and Physics of the Earth's Interior, Academic Press, New York.

Townley, S.D. (1939), Earthquakes in California, 1769 to 1928, *Bull. Seismol. Soc. Am.*, 29, 21-252.

Ulrich, F.P. (1941), The Imperial Valley Earthquakes of 1940, *Bull. Seismol. Soc. Am.*, 31, 13-31.

U.S. Geological Survey, the Southern California Earthquake Center, and the California Division of Mines and Geology (2000), Preliminary Report on the 16 October 1999 M7.1 Hector Mine, California, Earthquake, *Seismol. Res. Lett.*, 71, 11-23.

Ward, S.N. (1985), Quasi-static propagator matrices: creep on strike-slip faults, *Tectonophysics*, 120, 83-106.

Wdowinski, S., Y. Sudman, and Y. Bock (2001), Geodetic detection of active faults in S. California, *Geophys. Res. Lett*, 28, 2321-2324.

Weertman, J. (1964), Continuum distribution of dislocations on faults with finite friction, *Bull. Seismol. Soc. Am.*, 54, 1035-1058.

Williams, C.A., and R.M. Richardson (1991), A rheologically layered three-dimensional model of the San Andreas Fault in central and southern California, *J. Geophys. Res.*, 96, 16,597-16,623.

Wood, H.O. (1955), The 1857 earthquake of California, *Bull. Seismol. Soc. Am.* 45, 47-67.

Working Group on California Earthquake Probabilities (WGCEP) (1995), Seismic hazards in southern California: Probable earthquakes, 1994 to 2024, *Bull. Seismol. Soc. Am., 85*, 379-439.

Working Group on California Earthquake Probabilities (WGCEP) (1999), Earthquake probabilities in the San Francisco Bay Region: 2000 to 2030 – A summary of findings, *U.S. Geol. Surv. Open File Rep.,* [Online] *99-517,* version 1.0.

Working Group on California Earthquake Probabilities (WGCEP) (2003), Earthquake Probabilities in the San Francisco Bay Region: 2002-2031, *USGS Open File Report 03-214.*

Working Group on Northern California Earthquake Potential (WGNCEP) (1996), Database of potential sources for earthquakes larger than magnitude 6 in northern California, *U.S. Geol. Surv. Open File Rep., 96-705.*

Young, J.J., J.R. Arrowsmith, L. Colini, L.B. Grant, and B. Gootee (2002), Three-dimensional excavation and recent rupture history along the Cholame segment of the San Andreas fault, *Bull. Seismol. Soc. Am.*, 92, 2670-2688.

Yu, E., and P. Segall (1996), Slip on the 1868 Hayward earthquake from the analysis of historical trianulation data, *J. Geophys. Res*, 101, 16,101-16,118.

Yule, D. (2000), Neotectonic and paleoseismic investigation of the San Andreas Fault System, San Gorgoniao Pass, Annual Report, California State University Northridge.

Zeng, Y. (2001), Viscoelastic stress-triggering of the 1999 Hector Mine earthquake by the 1992 Landers earthquake, *Geophys. Res. Lett.*, 28, 3007-3010.

Figure Captions.

Figure 1. Historical earthquake ruptures (M ≥ 6.0) of the San Andreas Fault System from 1800-2004 [*Jennings*, 1994; *Toppozada et al*., 2002]. Colors depict era of earthquake activity from 1800-1850 (red), 1850-1900 (yellow), 1900-1950 (green), and 1950-2004 (blue). Calendar years corresponding to each rupture are also given and can be cross-referenced with Table 1. Note that we represent the two adjacent events of 1812 along the southern San Andreas as one event and that widths of highlighted fault ruptures are not proportional to earthquake magnitude. Although not directly occurring on the San Andreas Fault System, both 1992 Landers and 1999 Hector Mine events are also shown in the Eastern California Shear Zone (ECSZ). Grey octagons represent locations of paleoseismic sites used in this study. Letters a-s identify each site with the information in Table 2: (a) Imperial Fault, (b) Thousand Palms, (c) Burrow Flats, (d) Plunge Creek, (e) Pitman Canyon, (f) Hog Lake, (g) Wrightwood, (h) Pallet Creek, (i) Frazier Mountain, (j) Bidart Fan, (k) Las Yeguas, (l) Grizzly Flat, (m) Bolinas Lagoon, (n) Dogtown, (o) Olema, (p) Bodego Harbor, (q) Ft. Ross, (r) Point Arena, and (s) Tyson's Lagoon. Labeled fault segments referred to in the text include the Imperial, San Andreas, San Jacinto, Parkfield, Creeping section, and Hayward. Other locations that are referenced in the text include EC = El Centro, Br = Brawley, SJC = San Juan Capistrano, CP = Cajon Pass, SG = San Gabriel, SF = San Fernando, TP = Tejon Pass, V = Ventura, M = Monterey, SJB = San Juan Bautista, and Ok = Oakland.

Figure 2. San Andreas Fault System segment locations in the pole of deformation (PoD) coordinate system [*Wdowinski et al*., 2001 (52° N, 287° W)]. Fault segments coinciding with Table 3 are labeled and separated by grey circles. SOPAC station locations (red triangles) and USGS station locations (five networks, white triangles) used in this analysis are also shown.

Figure 3. 1000-year viscoelastic model parameter search results for elastic plate thickness (H), half-space viscosity (η), geologic Poisson's ratio (v_g), and locking depth factor (f_d). The best fitting model (unweighted RMS residual = 2.46 mm/yr, weighted RMS residual = 4.503) requires (a) H = 70 km, (b) $\eta = 3 \times 10^{18}$ Pa s, (c) $v_g = 0.4$, and (d) $f_d = 0.70$. Weighted RMS residuals for 50 example models are also plotted. Note that best-fit parameters are held constant in each figure for display purposes, although an actual 4-D parameter search used to derive the best fitting model.

Figure 4. (a) Fault-parallel (or *y*-component) velocity map of best fitting model. Velocities are plotted in mm/yr and span +20 mm on the west side of the SAF System and –20 mm on the east side of the SAF System. Dashed lines represent horizontal model profiles of Figure 4b. (b) Modeled velocity profiles acquired across the fault-parallel velocity map with GPS velocities and uncertainties projected onto each profile for visual comparison. GPS stations located within the half-way mark between each mapped profile line of (a) are displayed in each profile section of (b). Note that the RMS differences between model and date were evaluated at actual GPS locations.

Figure 5. (a) Fault-perpendicular (or *x*-component) velocity map of best fitting model. Velocities are plotted in mm/yr and span +/- 6 mm/yr. Negative velocities correspond to

displacement changes in the westward direction, while positive velocities correspond to displacement changes in the eastward direction. (b) Vertical (or z-component) velocity map of best fitting model. Velocities are plotted in mm/yr and span +/- 4 mm/yr. Negative velocities indicate subsidence, while positive velocities indicate uplift.

Figure 6. Coulomb stress in MPa for the SAF System for three model snapshots in time. (a) Coulomb stress for the 1811 calendar year model, representing the stress field prior to the 1812 M~7 Wrightwood Earthquakes (fault rupture estimated by black solid line). (b) Coulomb stress for the 1856 calendar year model, representing the stress field prior to the M7.9 1857 Great Fort Tejon Earthquake (epicenter represented by black star, fault rupture estimated by black solid line). (c) Coulomb stress for the 2004 calendar year model, representing stress of present day. Color scales range from –0.01 MPa, depicting stress shadow regions, to a saturated value of 3 MPa, depicting regions of accumulated stress.

Figure A1. 3-D sketch of Fourier fault-model simulating an elastic layer overlying a linear Maxwell viscoelastic half-space [*Smith and Sandwell*, 2004]. Fault elements are embedded in a plate of thickness H and extend from a lower depth of d_1 to an upper depth of d_2. A displacement discontinuity across each fault element is simulated using a finite width force couple, F, imbedded in a fine grid. Model parameters include plate velocity (V_o), shear modulus (μ_1, μ_2), Young's modulus (E_1, E_2), density (ρ), and viscosity (η).

Table Captions.

Table 1. Historical earthquakes of the San Andreas Fault System ($M \geq 6.0$) from 1800-2004 [*Jennings*, 1994; *Toppozada et al*., 2002]. The following moment abbreviations are used: M_w = moment magnitude, M_a = area-determined magnitude [*Toppozada and Branum*, 2002], M_s = surface-wave magnitude [*Toppozada et al*., 2002], and M_i = intensity magnitude [*Bakun and Wentworth*, 1997]. M_w is typically used for modern earthquake magnitudes, while M_a, M_s, and M_i are used for preinstrumentally estimated earthquake magnitudes.

Table 2. Prehistorical San Andreas Fault System earthquakes from 1000 A.D. based on paleoseismic trench excavations. Letters in the first column correspond to paleoseismic locations plotted in Figure 1. Trench site name, referenced authors, and calendar year event dates are also listed.

Table 3. San Andreas Fault System parameters. Slip rates are based on geodetic measurements, geologic offsets, and plate reconstructions [*WGCEP*, 1995, 1999] and satisfy an assumed far-field plate velocity of 40 mm/yr. Locking depths are based on the previous results of *Smith and Sandwell* [2003], although slight modifications have been made to the Superstition and South-Central segments (see text). Recurrence intervals (τ_r) for each segment were adopted from various sources [*WGCEP,* 1995, 1999; *WGNCEP*, 1996]. Calendar year rupture dates on fault segments, determined by historical events (Table 1) and prehistorical events (Table 2) are also included. SA = San Andreas segments, SJ = San Jacinto segments.

Movie Captions.

Movie 1. (a & b) 3-D deformation time series representing historical activity (1800 – 2004) of the San Andreas Fault System. A timescale (representing calendar years) is shown at the top while a time counter is also shown at the bottom corner of each image. Shown on the left is the *x*-component (or fault-perpendicular component, mm/yr) of velocity, in the center is the *y*-component (or fault-parallel component, mm/yr) of velocity, and on the right is the *z*-component (or vertical component, mm) of displacement. Note that the geologic, or secular, component of the vertical displacement model has been removed in order to isolate the vertical response associated with coseismic and postseismic displacements. Also note that both velocity models are plotted with a color scale that is wrapped, where velocity associated with each colored fringe is represented by the color scale. Both *x*- and *y*- velocity models maintain the background secular velocity through time, with the exception of the associated coseismic and small-magnitude transient postseismic response generated after each earthquake. The vertical displacement model shows migrating lobate patterns that form to the north and south of the Creeping segment due to the accumulating slip deficit since the 1857 and 1906 earthquakes. A repeating 1857-like rupture, for example, would significantly reduce the magnitude of this feature in southern California observed in years leading up to 2004. If we were to isolate this segment and rupture scenario entirely and allow it to relax completely, over multiple earthquake cycles we would observe this vertical feature as it completely diminishes to zero. While this animation only reveals deformation over the past 200 years, it is important to note that both velocity and displacements from events occurring over the past 1000 years are captured in this animation. Note: (a) slow animation, insightful for viewing *x*-and *y*-velocity components. (b) fast animation, insightful for viewing *z*-displacement component.

Movie 2. (a & b) Coulomb Stress time series representing historical activity (1800 – 2004) of the San Andreas Fault System. A timescale (representing calendar years) is shown at the top while a time counter is also shown at the bottom corner the image. Regions of high stress (red, > 2 MPa) and stress shadows (purple, < 0.01 MPa) accumulate and decay, respectively, with time. Note the accumulating stress over the central section of the San Andreas just prior to 1857. Likewise, note a similar scenario leading up the 1906 San Francisco event in northern California. While this animation only reveals stress behavior over the past 200 years, it is important to note that stress accumulation and release from events occurring over the past 1000 years are captured in this animation. Note: (a) slow animation (b) fast animation.

Figure 1

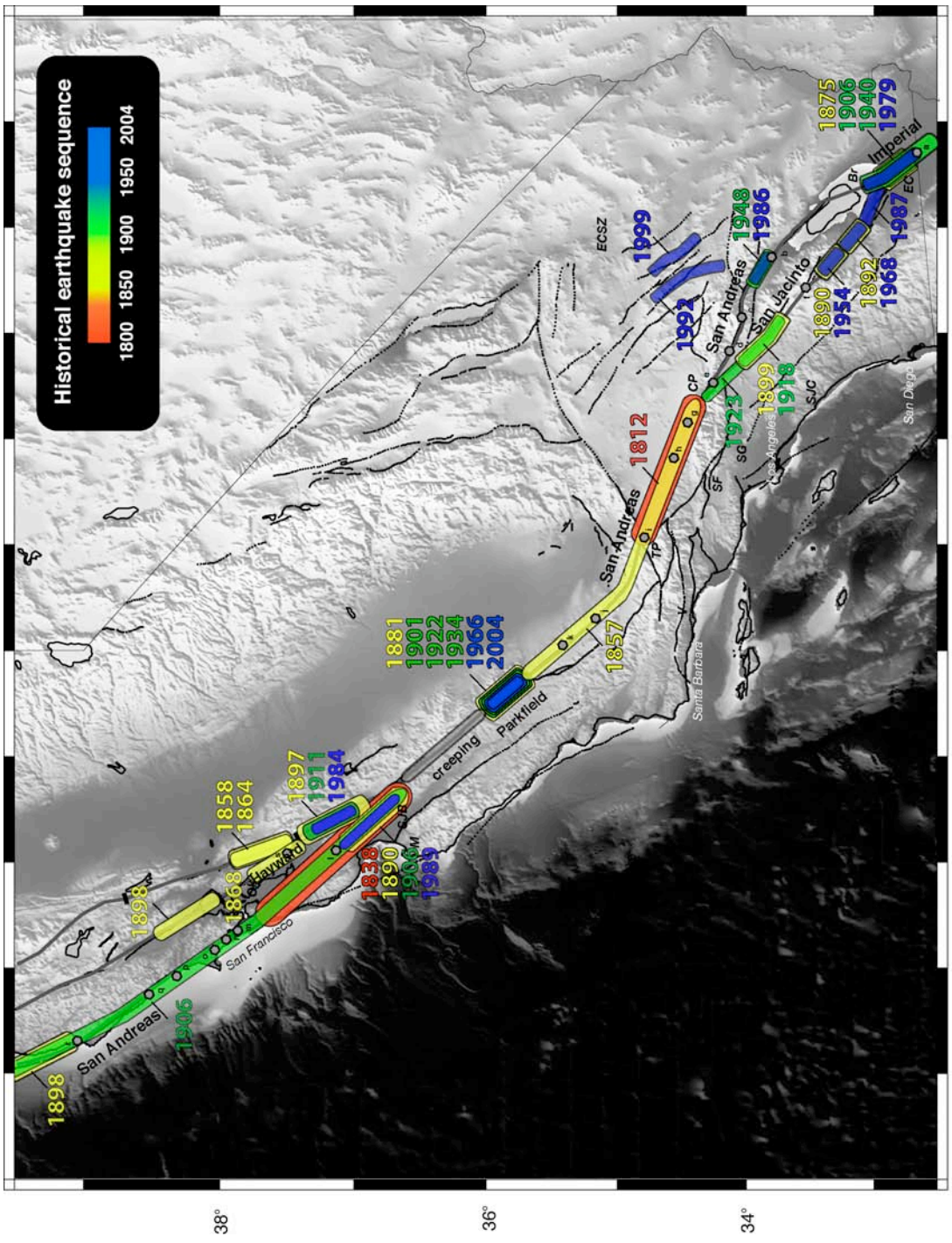
Historical earthquake sequence
1800 1850 1900 1950 2004
San Andreas
San Francisco
Hayward
creeping
Parkfield
San Andreas
Santa Barbara
San Andreas
San Jacinto
Imperial
ECSZ
1898
1906
1868
1858
1864
1838
1890
1906
1989
1897
1911
1984
1881
1901
1922
1934
1966
2004
1857
1812
1923
1899
1918
1992
1999
1948
1986
1875
1906
1940
1979
1890
1954
1892
1968
1987
38°
36°
34°
-124°
-122°
-120°
-118°
-116°

Figure 2

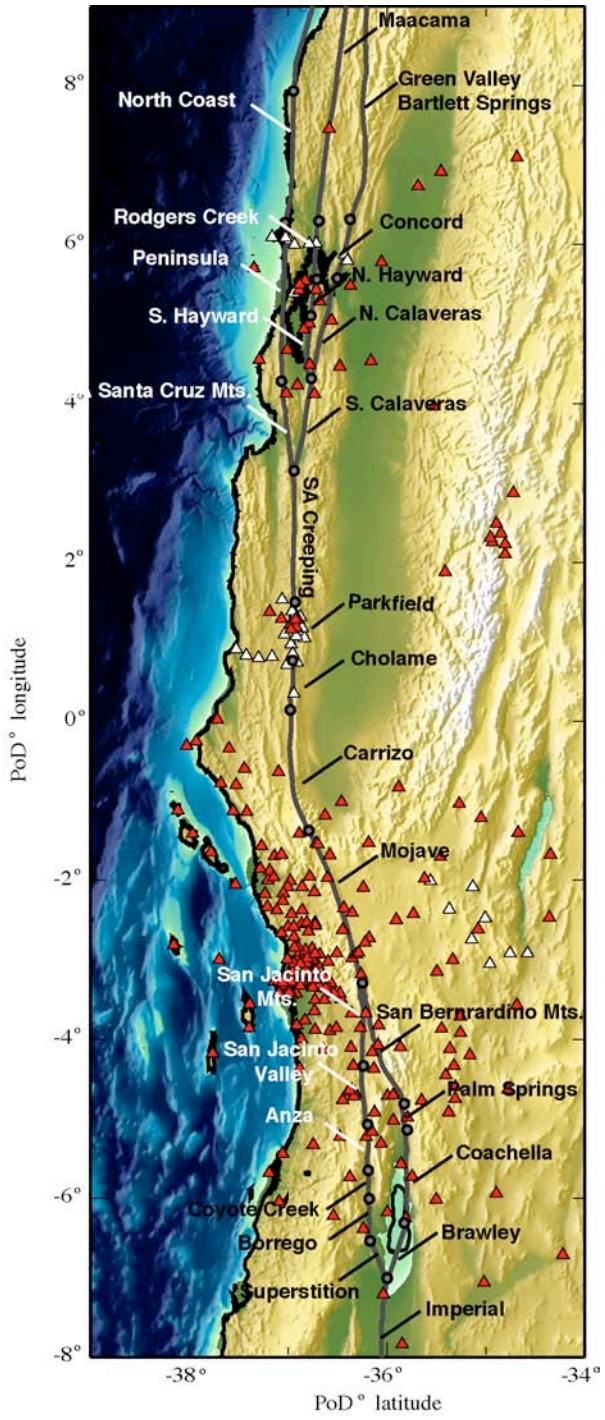
Maacama
Green Valley
Bartlett Springs
North Coast
Rodgers Creek
Concord
Peninsula
N. Hayward
S. Hayward
N. Calaveras
Santa Cruz Mts.
S. Calaveras
SA Creeping
Parkfield
Cholame
Carrizo
Mojave
San Jacinto Mts.
San Bernardino Mts.
San Jacinto Valley
Palm Springs
Anza
Coachella
Coyote Creek
Brawley
Borrego
Superstition
Imperial
8°
6°
4°
2°
0°
-2°
-4°
-6°
-8°
-38°
-36°
-34°
PoD ° longitude
PoD ° latitude

Figure 3

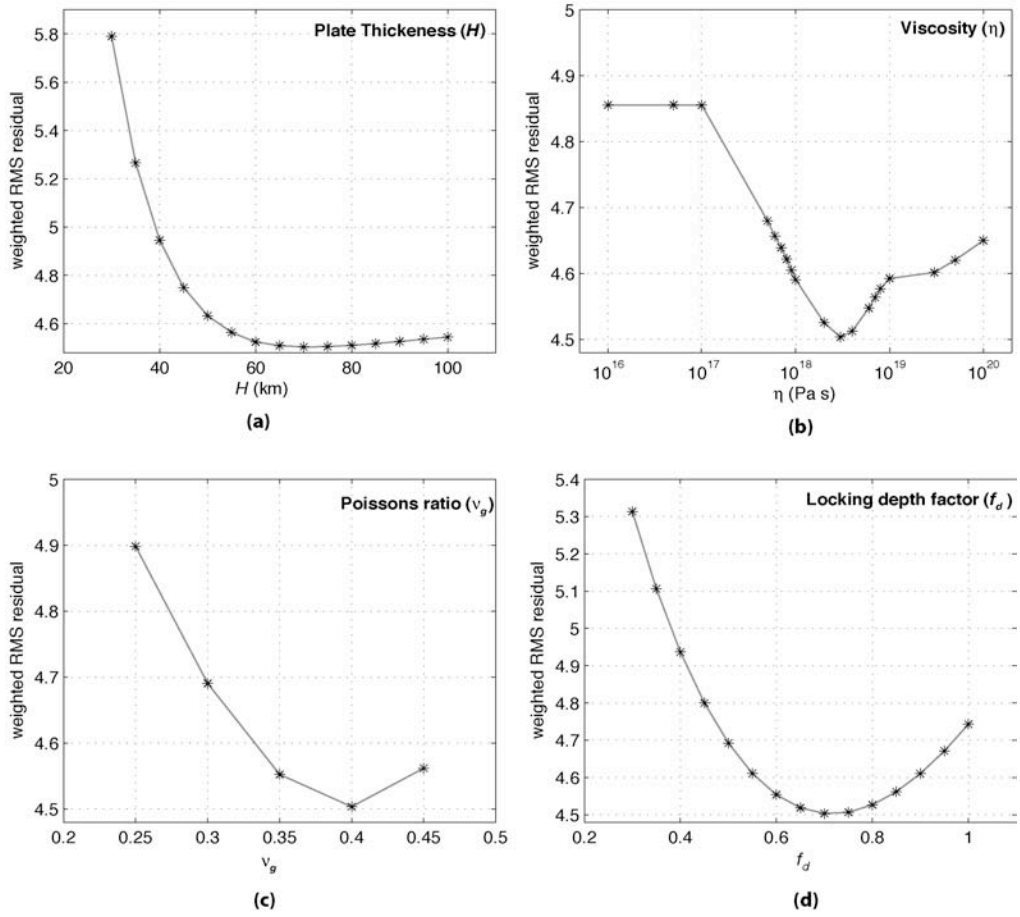
Plate Thickeness (H)
weighted RMS residual
H (km)
(a)
Viscosity (η)
η (Pa s)
(b)
Poissons ratio (ν_g)
ν_g
(c)
Locking depth factor (f_d)
f_d
(d)

Figure 4

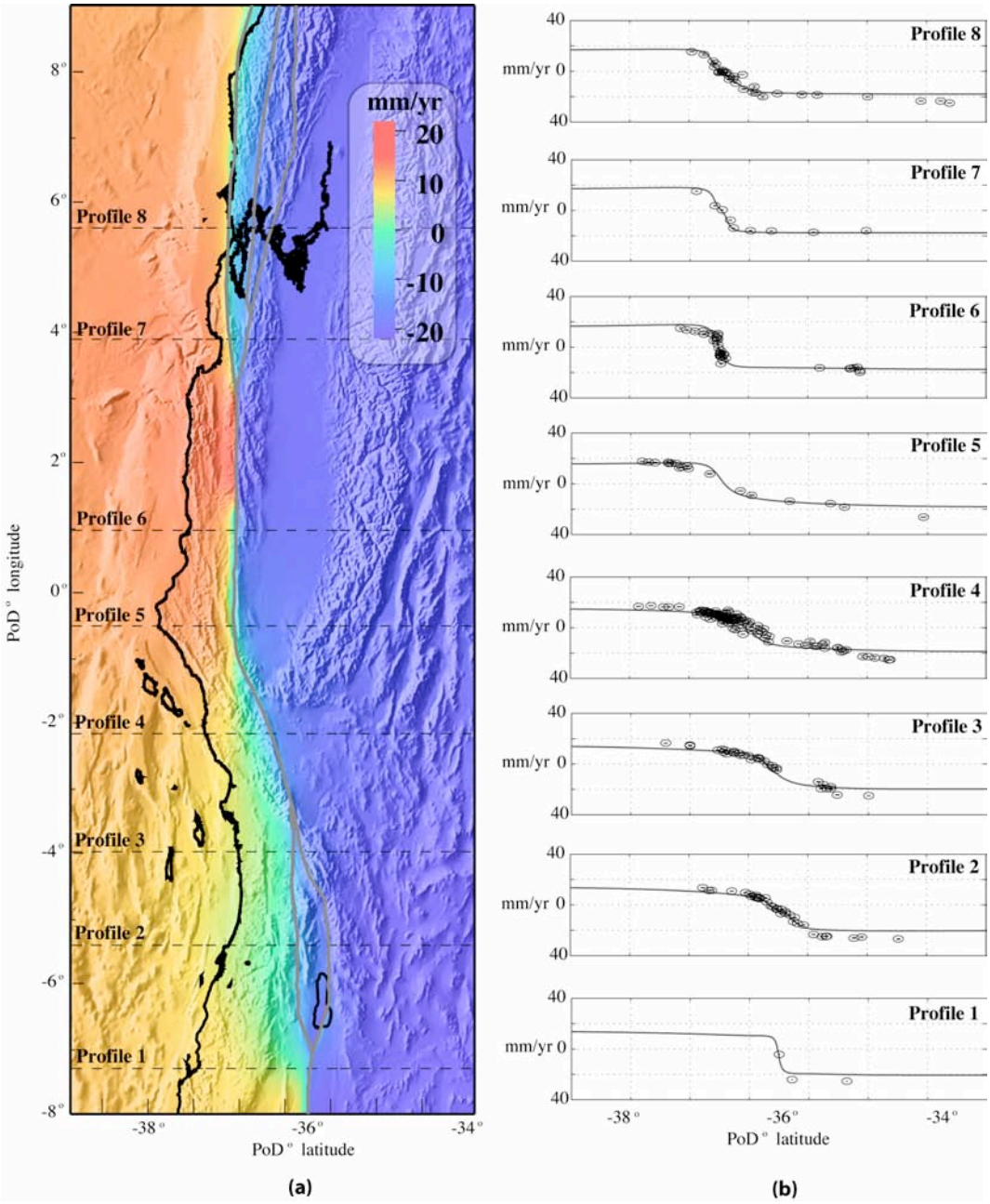
mm/yr
20
10
0
-10
-20
Profile 8
Profile 7
Profile 6
Profile 5
Profile 4
Profile 3
Profile 2
Profile 1
8°
6°
4°
2°
0°
-2°
-4°
-6°
-8°
-38°
-36°
-34°
PoD ° longitude
PoD ° latitude
(a)
40
mm/yr 0
40
(b)

Figure 5

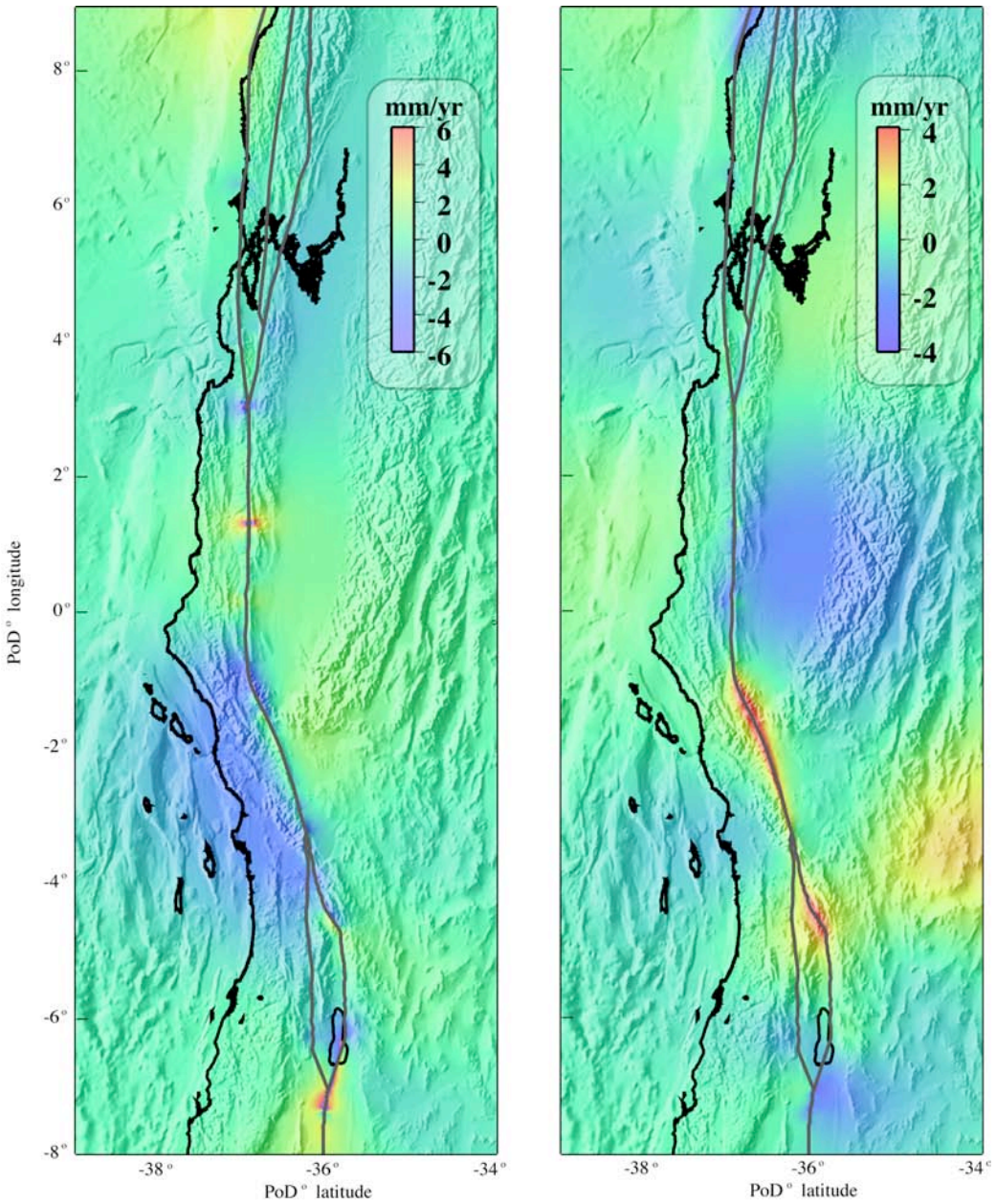
mm/yr
6
4
2
0
-2
-4
-6
8°
6°
4°
2°
0°
-2°
-4°
-6°
-8°
PoD° longitude
-38°
-36°
-34°
PoD° latitude
(a)
mm/yr
4
2
0
-2
-4
-38°
-36°
-34°
PoD° latitude
(b)

Figure 6

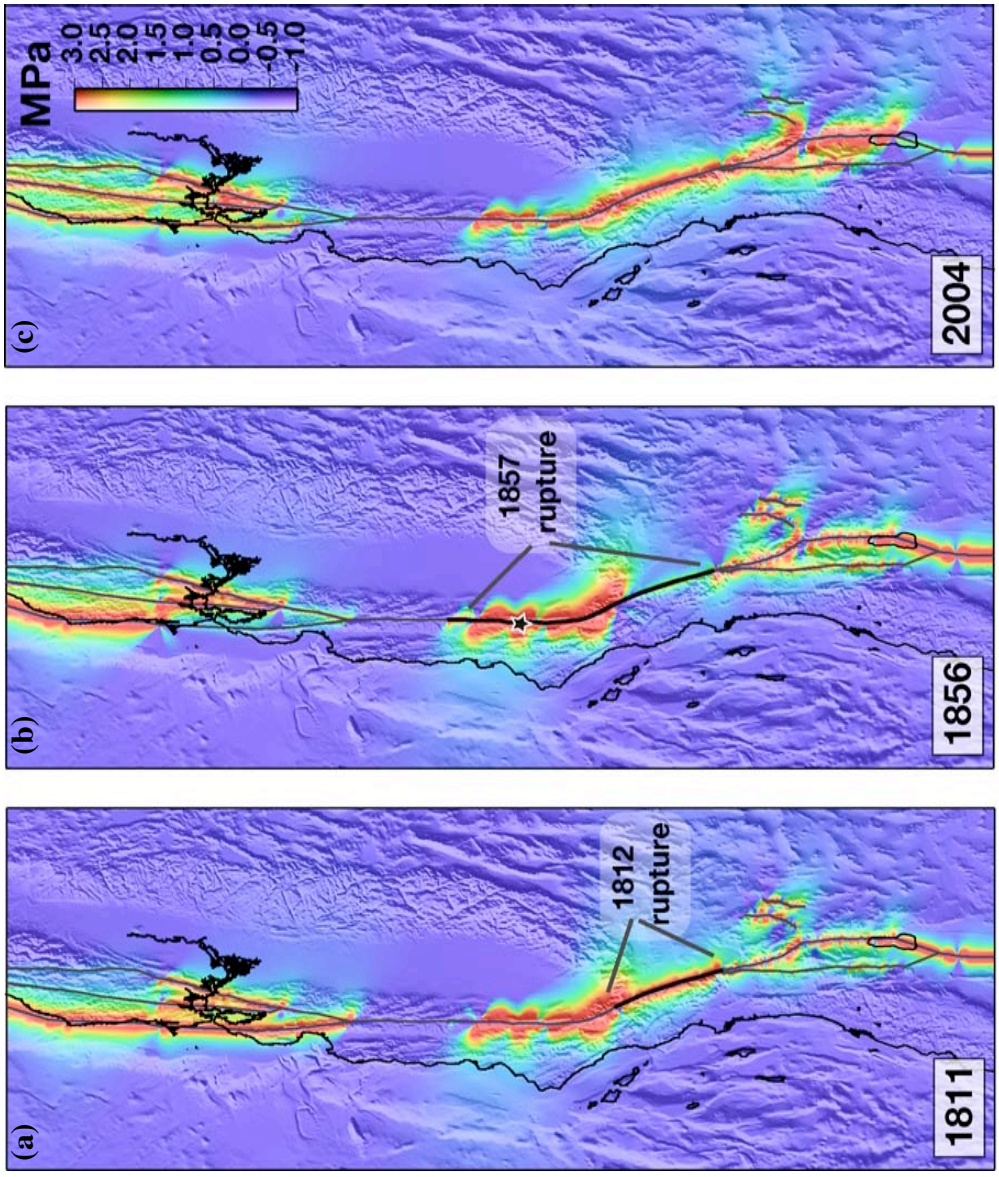
MPa
3.0
2.5
2.0
1.5
1.0
0.5
0.0
-0.5
-1.0
(c)
2004
(b)
1857
rupture
1856
(a)
1812
rupture
1811

Figure A1

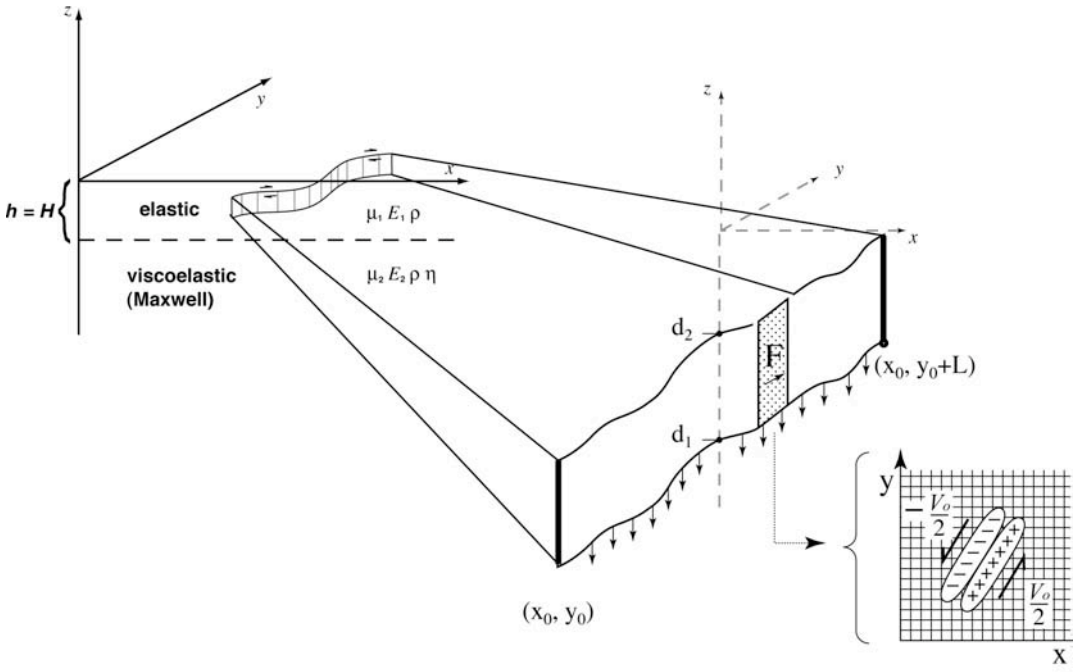
z
y
h = H
elastic
μ1 E1 ρ
viscoelastic
(Maxwell)
μ2 E2 ρ η
x
z
y
x
d2
d1
F
(x0, y0+L)
(x0, y0)
y
x
V0/2
V0/2

Table 1. Historical earthquakes of the San Andreas Fault System ($M \geq 6.0$) from 1800-2004 [*Jennings*, 1994; *Toppozada et al*., 2002]. The following moment abbreviations are used: M_w = moment magnitude, M_a = area-determined magnitude [*Toppozada and Branum*, 2002], M_s = surface-wave magnitude [*Toppozada et al.*, 2002], and M_i = intensity magnitude [*Bakun and Wentworth*, 1997]. M_w is typically used for modern earthquake magnitudes, while M_a, M_s, and M_i are used for preinstrumentally estimated earthquake magnitudes.

Year	Event name	Magnitude
1812	Wrightwood	M_w 7.5
1838	San Francisco	M_a 7.4
1857	Fort Tejon	M_w 7.9
1858	East Bay Area	M_a 6.2
1864	East Bay Area	M_a 6.1
1864	Calaveras	M_a 6.1
1868	South Hayward	M_w 7.0
1875	Imperial Valley	M_i 6.2
1881	Parkfield	M_a 6.0
1890	S. San Jacinto	M_w 6.8
1890	Pajaro Gap	M_a 6.3
1892	S. San Jacinto	M_a 6.5
1897	Gilroy	M_a 6.3
1898	Mare Island	M_a 6.4
1898	Fort Bragg-Mendicino	M_s 6.7
1899	San Jacinto/Hemet	M_w 6.7
1901	Parkfield	M_s 6.4
1906	San Francisco	M_w 7.8
1906	Imperial Valley	M_w 6.2
1911	SE of San Jose	M_w 6.4
1918	San Jacinto	M_w 6.8
1922	Parkfield	M_w 6.3
1923	N. San Jacinto	M_w 6.2
1934	Parkfield	M_w 6.0
1940	Imperial Valley	M_w 7.0
1948	Desert Hot Springs	M_w 6.0
1954	Arroyo Salado	M_w 6.3
1966	Parkfield	M_w 6.0
1968	Borrego Mountain	M_w 6.6
1979	Imperial Valley	M_w 6.5
1984	Morgan Hill	M_w 6.2
1986	N. Palm Springs	M_w 6.0
1987	Superstition Hills	M_w 6.6
1989	Loma Prieta	M_w 6.9
1992	Landers	M_w 7.3
1999	Hector Mine	M_w 7.1
2004	Parkfield	M_w 6.0

Table 2. Prehistorical San Andreas Fault System earthquakes from 1000 A.D. based on paleoseismic trench excavations. Letters in the first column correspond to paleoseismic locations plotted in Figure 1. Trench site name, referenced authors, and calendar year event dates are also listed.

	Trench Site	Reference	Dates (A.D)
a	**Imperial Fault**	*Thomas and Rockwell,* 1996; *Sharp,* 1981	< 1700; 1670
b	**Thousand Palms**	*Fumal et al.,* 2002	> 1520-1680; 1450-1555; 1170-1290; 840-1150
c	**Burrow Flats**	*Yule,* 2000	1450-1600; 1120-1350; 780-1130
d	**Plunge Creek**	*McGill et al.,* 2002	1690; 1630; 1450
e	**Pitman Canyon**	*McGill et al.,* 2002	~1450
f	**Hog Lake**	*Rockwell et al.,* 2003	1020; 1230; 1290; 1360; 1630; 1760
g	**Wrightwood**	*Fumal et al.,* 2002; *Biasi et al.,* 2002	1647-1717; 1508-1569; 1448-1578; 1191-1305; 1047-1181
h	**Pallet Creek**	*Biasi et al.,* 2002	1496-1599; 1343-1370; 1046-1113; 1031-1096
i	**Frazier Mountain**	*Lindevall et al.,* 2002	1460-1600
j	**Bidart Fan**	*Grant and Sieh,* 1994	1405-1510; 1277-1510; 1218-1276
k	**Las Yeguas (LY4)**	*Young et al.,* 2002	1030-1460
l	**Grizzly Flat**	*Schwartz et al.,* 1998; *Heingartner,* 1998	1020-1610; 1430-1670
m	**Bolinas Lagoon**	*Knudsen et al.,* 2002	1050-1450
n	**Dogtown**	*Cotton et al.,* 1982	1100-1330; 1520-1690
o	**Olema**	*Niemi and Hall,* 1992; *Niemi,* 1992	1300-1660; 1560-1660
p	**Bodego Harbor**	*Knudsen et al.,* 2002	900-1390; 1470-1850
q	**Ft. Ross**	*Noller,* 1993; *Simpson et al.,* 1996	560-950; 920-1290; 1170-1650
r	**Point Arena**	*Prentice,* 1989; *Baldwin,* 1996	680-1640; 1040-1640
s	**Tyson's Lagoon**	*Lienkamper et al.,* 2002	1650-1790; 1530-1740; 1360-1580

Table 3. San Andreas Fault System parameters. Slip rates are based on geodetic measurements, geologic offsets, and plate reconstructions [*WGCEP*, 1995, 1999] and satisfy an assumed far-field plate velocity of 40 mm/yr. Locking depths are based on the previous results of *Smith and Sandwell* [2003], although slight modifications have been made to the Superstition and South-Central segments (see text). Recurrence intervals (τ_r) for each segment were adopted from various sources [*WGCEP*, 1995, 1999; *WGNCEP*, 1996]. Calendar year rupture dates on fault segments, determined by historical events (Table 1) and prehistorical events (Table 2) are also included. SA = San Andreas segments, SJ = San Jacinto segments.

Segment Name	Slip	Locking depth	τ_r	Historical Earthquakes	Prehistorical Earthquakes
	(mm/yr)	(km)	(yrs)	(calendar year)	(calendar year)
Imperial	40	6	40	1875, 1906, 1940, 1979	1680
Brawley	36	6	48		
Coachella (SA)	28	23	160		1350, 1690
Palm Springs (SA)	28	23	160	1948, 1986	1110, 1502, 1690
San Bernardino Mountains (SA)	28	23	146		1450, 1630, 1690
Superstition (SJ)	4	7	250	1987	
Borrego (SJ)	12	13	175	1892, 1968	
Coyote Creek (SJ)	12	13	175	1890, 1954	
Anza (SJ)	12	13	250		1020, 1230, 1290, 1360, 1630, 1760
San Jacinto Valley (SJ)	12	13	83	1899, 1918	
San Jacinto Mountains (SJ)	12	13	100	1923	
Mojave	40	26	150	1812, 1857	1016, 1116, 1263, 1360, 1549, 1685
Carrizo	40	25	206	1857	1247, 1393, 1457
Cholame	40	13	140	1857	1195
Parkfield Transition	40	15	25	1881, 1901, 1922, 1934, 1966, 2004	
San Andreas Creeping	40	0	n/a		
Santa Cruz Mountains (SA)	21	9	400	1838, 1890, 1906, 1989	1300, 1600
San Francisco Peninsula (SA)	21	9	400	1838, 1906	1300, 1600
San Andreas North Coast (SA)	25	19	760	1906	1300, 1600
South-Central Calaveras	19	7	60	1897, 1911, 1984	
North Calaveras	7	14	700	1858, 1864	
Concord	7	14	700		
Green Valley-Bartlett Springs	5	9	230		
South Hayward	12	16	525	1868	1470, 1630, 1730
North Hayward	12	16	525		1708
Rodgers Creek	12	19	286	1898	
Maacama	10	12	220		